

Alma Mater Studiorum Università di Bologna
Archivio istituzionale della ricerca

A geology-based 3D velocity model of the Amatrice Basin (Central Italy)

This is the final peer-reviewed author's accepted manuscript (postprint) of the following publication:

Published Version:

Livani M., Scrocca D., Gaudiosi I., Mancini M., Cavinato G.P., de Franco R., et al. (2022). A geology-based 3D velocity model of the Amatrice Basin (Central Italy). *ENGINEERING GEOLOGY*, 306, 1-16 [10.1016/j.enggeo.2022.106741].

Availability:

This version is available at: <https://hdl.handle.net/11585/899022> since: 2024-05-24

Published:

DOI: <http://doi.org/10.1016/j.enggeo.2022.106741>

Terms of use:

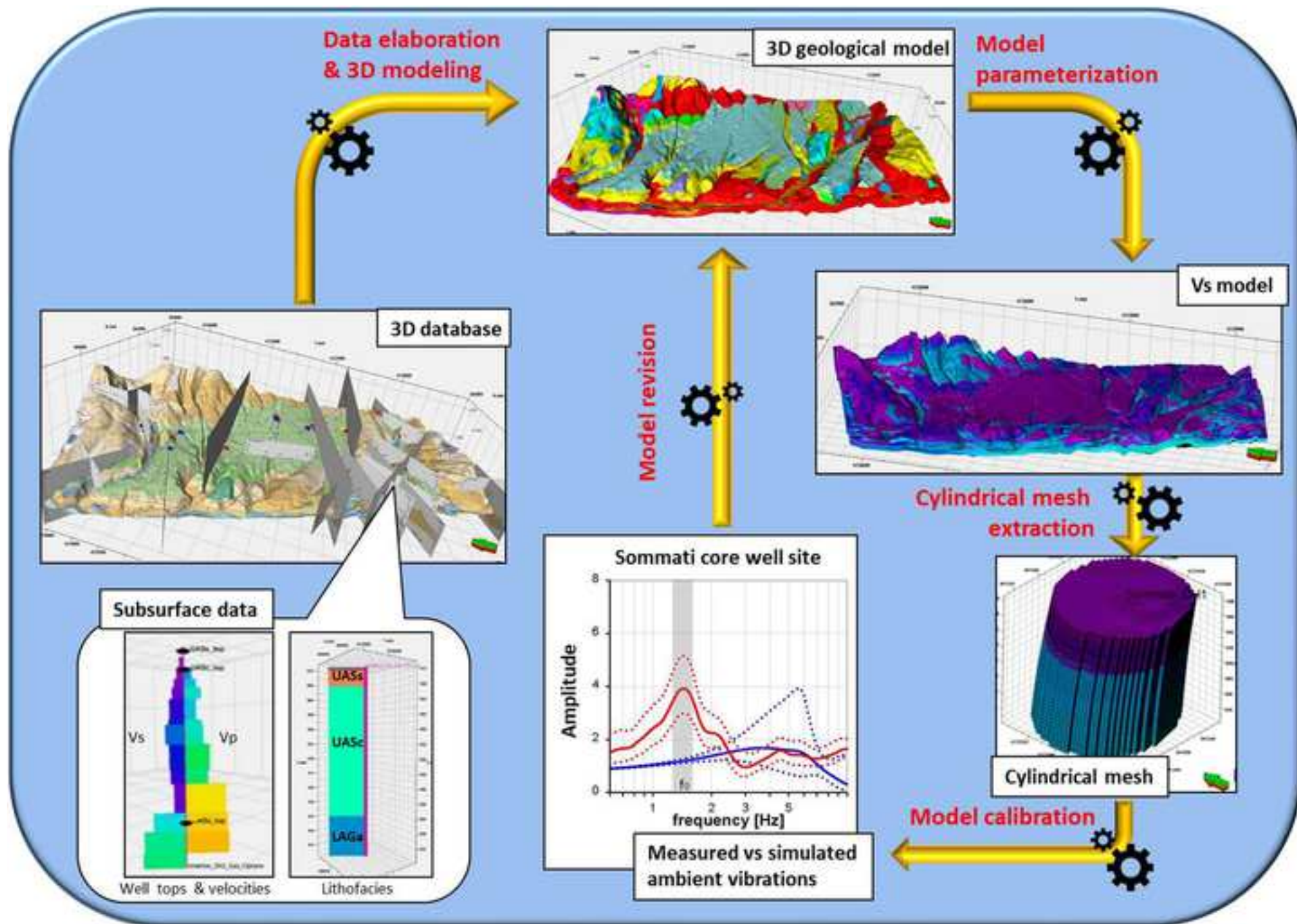
Some rights reserved. The terms and conditions for the reuse of this version of the manuscript are specified in the publishing policy. For all terms of use and more information see the publisher's website.

This item was downloaded from IRIS Università di Bologna (<https://cris.unibo.it/>).
When citing, please refer to the published version.

(Article begins on next page)

Highlights

- A new detailed 3D geological model, with related geophysical parameters, of the uppermost hundreds of meters of the Amatrice area has been elaborated;
- the model has been calibrated by processing the ellipticity curves of the Rayleigh fundamental mode at four chosen sites;
- the model predicts correctly the amplitude and frequency of arriving waves;
- the model could help in predicting possible focusing and/or amplification effects due to the morpho-litho-stratigraphic setting of the near surface geological structures;
- the proposed modeling approach allows to define more realistic seismic hazard scenarios being also exploitable in other similar seismic areas.



1 **3D geological modeling, a new approach in seismic hazard assessment studies: insights**
2 **from the Amatrice case study (central Italy).**
3

4 **Michele Livani^a, Davide Scrocca^{a,*}, Iolanda Gaudiosi^b, Marco Mancini^b, Gian Paolo**
5 **Cavinato^a, Roberto de Franco^c, Grazia Caielli^c, Gianluca Vignaroli^{b,d}, Alessandro Romi^e,**
6 **Massimiliano Moscatelli^b.**

7 ^a Istituto di Geologia Ambientale e Geoingegneria, Consiglio Nazionale delle Ricerche, c/o
8 Dipartimento di Scienze della Terra, Università Sapienza, P. le A. Moro 5 - 00185, Roma, Italy

9 ^b Istituto di Geologia Ambientale e Geoingegneria, Consiglio Nazionale delle Ricerche, Area della
10 Ricerca di Roma 1, Strada Provinciale 35d 9 - 00010, Montelibretti (RM), Italy

11 ^c Istituto di Geologia Ambientale e Geoingegneria, Consiglio Nazionale delle Ricerche, Piazza della
12 Scienza,1 - 20126 Milano, Italy

13 ^d Dipartimento di Scienze Biologiche, Geologiche e Ambientali, Università degli Studi di Bologna,
14 Via Zamboni 67 - 40127, Bologna, Italy

15 ^e Schlumberger Italiana, Via dell'Unione Europea, 4 - Torre Beta 20097 San Donato Milanese (MI),
16 Italy

17

18 ***Corresponding author: Davide Scrocca**

19 E-mail: davide.scrocca@igag.cnr.it

20

21 *Abstract*

22 The Amatrice area (central Italy) falls in a high seismic hazard region, which has been struck by
23 several disastrous earthquakes. The recent 2016-2017 seismic sequence, with several earthquakes of
24 magnitude M_w greater than 5, caused extensive damage and 299 victims, reaffirming the
25 importance of activities devoted to the seismic risk prevention in an effective territorial planning.
26 In this paper we present a detailed 3D geological model, with related geophysical parameters, of the
27 uppermost hundreds of meters (maximum depth about 200 meters) of the Amatrice Basin subsoil.
28 Geological maps, cross-sections, and morphological data (Digital Elevation Model) have been
29 integrated with subsurface geological and geophysical data (e.g., core-well data and seismic noise
30 measures) and models obtained by the interpretation of surface and well geophysical measurements,
31 like S-wave (V_s) and P-wave (V_p) velocities. All data have been georeferenced and uploaded into a
32 3D geological modeling software, where faults, stratigraphic boundaries and geophysical attributes
33 have been digitized, checked, hierarchized, and modeled. A posteriori calibration of the 3D
34 reconstructed model has been operated by comparing the modeled seismic responses of some
35 extracted volumes with those obtained by environmental noise measurements (i.e., Horizontal-to-
36 Vertical Spectral Ratio analysis, HVSR). The final 3D model correctly reproduces the amplitude
37 and frequency of arriving waves in the Amatrice area, thus allowing an evaluation of possible
38 focusing and/or amplification effects due to the morpho-litho-stratigraphic setting of the near
39 surface geological features (i.e., Quaternary cover deposit and pre-Quaternary rocky substratum).
40 The proposed 3D modeling approach represents a promising general methodology for developing
41 more realistic seismic hazard scenario, useful for allowing an effective territorial planning.

42 **Keywords:** 3D geological model, seismic hazard assessment, seismic risk prevention, Amatrice
43 Basin, Laga Basin, central Apennines.

44 1 Introduction

45 In last decades, the advent of the three-dimensional (3D) geological modeling software gave to
46 geologists a new tool to effectively represent the subsurface. A detailed 3D geological and
47 mechanical model is an important tool for assessing the seismic hazard of an area. As an example,
48 compared to classic two-dimensional (2D) models, 3D seismogenic source models can provide a
49 more realistic prediction of the expected ground shaking as well as of its spatial distribution (e.g.,
50 Boncio et al., 2004). Defining 3D geometries of rock bodies and the spatial distribution of their
51 mechanical properties allow running physically based numerical simulations (e.g., Mazzieri et al.,
52 2013; Smerzini and Pitilakis, 2018) and, consequently, investigating their role in influencing the
53 upward propagation of seismic waves, highlighting the possible occurrence of focusing, reflection,
54 refraction and/or amplification effects. In addition, a 3D geological model can be used for
55 predicting amplitude and frequency of the arriving seismic waves (e.g., Magistrale et al., 1996; Süs
56 et al., 2001),

57 In this framework, our study area (the Amatrice Basin, central Italy), provides a remarkably
58 interesting case study for reconstructing a 3D geological model due to the large amount of
59 available seismological, geological and geophysical data. The Amatrice Basin (Cacciuni et al.,
60 1995; Vignaroli et al., 2019) is a NW-SE-trending intermountain depression in the axial part of the
61 central Apennines (Fig. 1). For this area, at the state of art, a 3D fully parameterized model in terms
62 of mechanical parameters is still missing.

63 The study area has been historically affected by moderate-to-large earthquakes that produced
64 extensive damage and many victims (e.g., the 1639 and 2016-2017 seismic sequences; Tiberi
65 Romano, 1639; Galli et al., 2016; Chiaraluce et al., 2017; Pizzi et al., 2017; Rovida et al., 2019; and
66 references therein) (Fig. 1). Recently, it has been struck by a seismic sequence started on the 24th
67 August 2016 (with the Amatrice earthquake of magnitude Mw 6.0) due to the activation of a
68 complex system of extensional faults. Numerous earthquakes of magnitude Mw > 5 have been
69 recorded in the period between 24th August 2016 and 18th January 2017 (e.g., Chiaraluce et al.,
70 2017; Improta et al., 2019; Michele et al., 2020 and references therein).

71 After the 2016-2017 events, the Amatrice area has been the subject of numerous research projects,
72 including surface geological surveying and data collection (e.g., V_s and V_p data) activities (e.g.,
73 Vignaroli et al., 2019; 2020; Mancini et al., 2020) aimed at the seismic microzonation (EmerTer
74 Project Working Group, 2018; Chiaretti & Nibbi, 2018). Seismic microzonation provided seismic
75 hazard estimates at the municipality scale, based on shallow geological/geotechnical conditions and
76 site-dependent constraints, for the design of new settlements and for interventions of retrofit and
77 reconstruction (Hailemikael et al., 2020). Furthermore, a 2D and 3D numerical modeling of the site

78 effects for the main hamlet of the entire Amatrice municipality has been also attempted (Gaudiosi et
79 al, 2021; Moscatelli et al., 2020; Razzano et al., 2020), while a new 3D geological modeling
80 project, named RETRACE-3D, has been launched. The latter aimed at obtaining, by interpreting
81 seismic lines and well data, a 3D seismotectonic and stratigraphic characterization of the Amatrice
82 Basin (Di Bucci et al., 2021; RETRACE-3D Working Group, 2021).

83 The aim of our study is to contribute to a more effective seismic hazard assessment of the Amatrice
84 area by providing an accurate (resolution from 5m up to 1m in-depth and 5m in plan) 3D geological
85 and mechanical model of a shallow portion (maximum depth about 200 meters) of subsoil, joining
86 the previously available existing models. Our model integrates surface and subsurface (some
87 hundred meters deep) geological data, as well as geophysical parameters, setting the ground for a
88 proper evaluation of the local seismic response in tectonically active geologically complex areas.
89 The methodology here proposed could bridge the gap between deep seismotectonic reconstructions
90 typical of seismic zonation and characterizations of shallow portions of subsoil in seismic
91 microzonation studies.

92

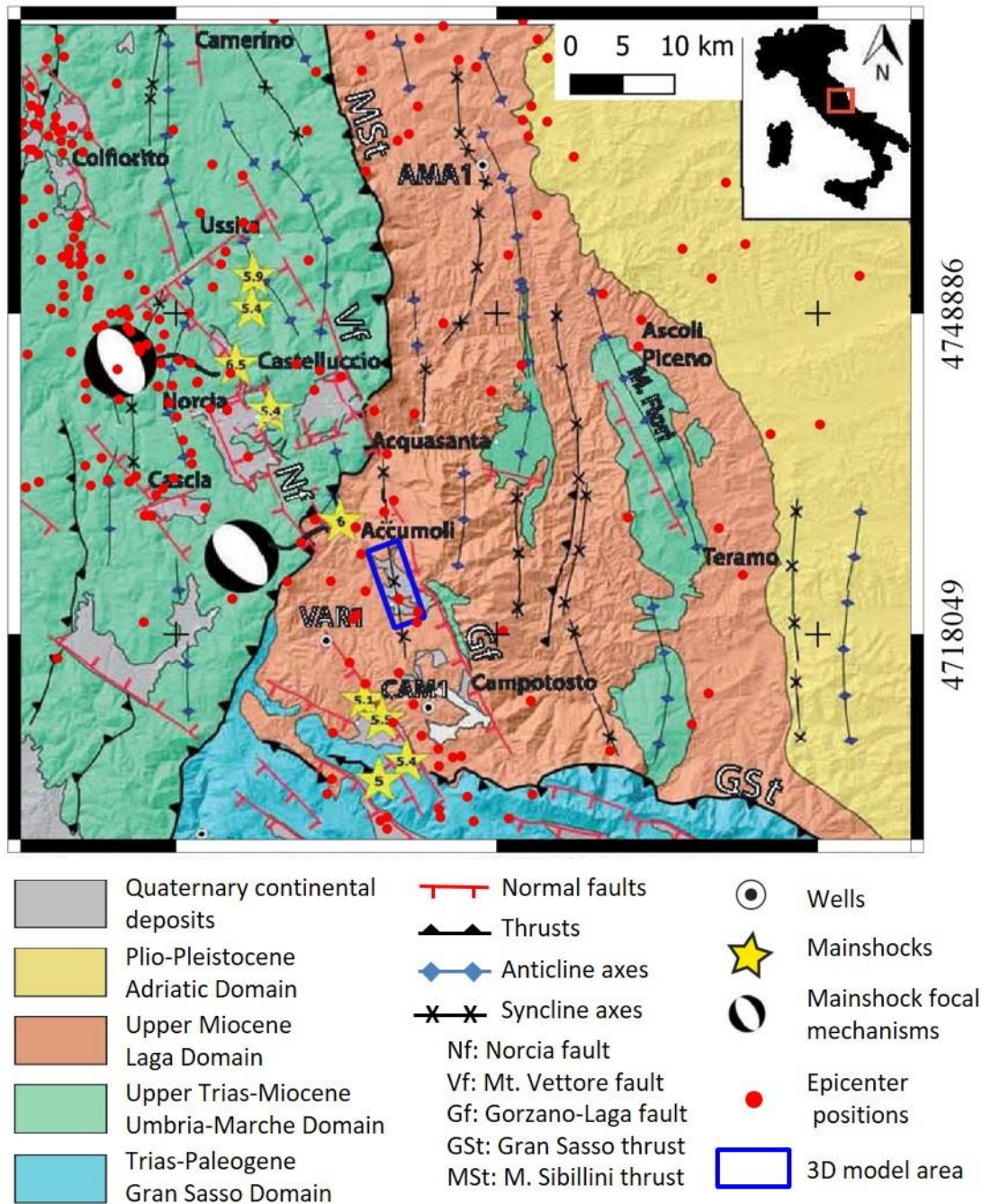
93 **2 Geological setting**

94 The study area is part of the central Apennines, an eastward-migrating fold-and-thrust belt,
95 developed since the upper Oligocene above the westward subducting Adria plate (Malinverno &
96 Ryan, 1986; Ricci Lucchi, 1986; Patacca et al., 1990; Boccaletti et al., 1990; Doglioni, 1991;
97 Argnani & Ricci Lucchi, 2001; Cosentino et al., 2010). Along the belt axial zone, the foredeep Laga
98 Basin is located, which is bounded by the Gran Sasso thrust to the south, the Sibillini thrust to the
99 west, and the Montagna dei Fiori-Montagnone anticline to the east (Fig. 1).

339207

370044

400881



100

101

102 **Figure 1:** Geological and seismicity map of the study area (modified after Porreca et al., 2018). Yellow stars represent
 103 the epicenter positions of the 2016 seismic event with $M_w > 5$. The focal mechanisms mainshocks (M_w 6.0 and 6.5) and
 104 the positions of the Amatrice 1 (AMA1), Campotosto 1 (CAM1) and Varoni 1 (VAR1) wells are shown. The position of the
 105 Gran Sasso and Sibillini regional thrusts (GSr and MSt, respectively), and of the Vettore (Vf), Norcia (Nf), and Gorzano-
 106 Laga (Gf) extensional fault systems are also shown. The blue rectangle indicates the Amatrice area, which is detailed in
 107 figure 4.

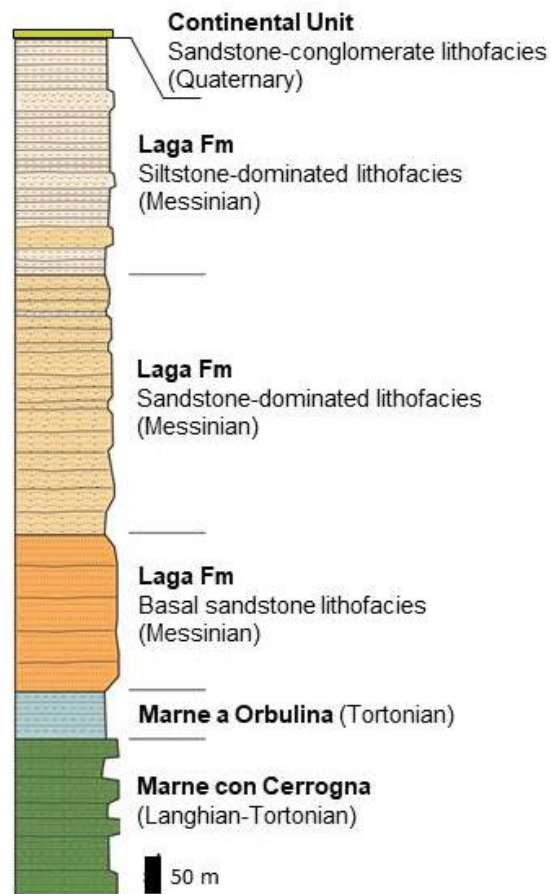
108

109 Facies and physical stratigraphy, analysis of thermal history, seismic line interpretations and
 110 balanced cross sections allowed a detailed reconstruction of the stratigraphy and the time-space

111 evolution of the Laga Basin, thus representing a key area to understand the most recent evolution of
112 the central Apennines (Koopman, 1983; Centamore et al., 1991; 1992; Artoni, 2003, 2007;
113 Moscatelli, 2003; Moscatelli et al., 2004; Scisciani & Montefalcone, 2005; Casero & Bigi, 2006;
114 Bigi et al., 2006, 2009; Stanzione et al., 2006; Aldega et al., 2007; Milli et al., 2007, 2009;
115 Cosentino et al., 2010).

116 The Laga Basin is filled by more than 2000-m thick deep-sea turbidite succession, named Laga
117 Formation (Mutti & Ricci Lucchi, 1972; Mutti et al., 1978; Mutti & Sonnino, 1981; Milli et al.,
118 2007, 2009; Marini et al., 2015, 2016). It consists of an alternation of lithofacies that vary from
119 arenaceous and pelitic-arenaceous to marly (e.g., Milli et al., 2007; 2009; Mancini et al., 2020)
120 grouped into three main members: pre-evaporitic (upper Tortonian-lower Messinian), evaporitic
121 (middle Messinian), and post-evaporitic (upper Messinian) ones (Roveri et al., 2001).

122 A 1200-m thick pre-evaporitic Laga Formation has been identified by the stratigraphy of the
123 Campotosto 1 and Varoni 1 wells (locations in figure 1) and the interpretation of some seismic
124 reflection profiles (e.g., Bigi et al., 2011; Porreca et al., 2018). The Laga Formation lies above the
125 “*Marne con Cerrognola*” and “*Marne ad Orbulina*” Formations, a Langhian to lower Messinian
126 pelagic succession that is today exposed at the footwall of the Gorzano-Laga Fault (in the eastern
127 edge of the study area) (Fig. 1). The Laga Formation is topped by a succession of lower Pleistocene
128 to Holocene continental deposits consisting of sandstones and conglomerates of alluvial fans and
129 fluvial terraces, forming the Amatrice Basin (e.g., Centamore et al., 1991, 1992; Cacciuni et al.,
130 1995; Vignaroli et al., 2019; 2020; Mancini et al., 2020) (Fig. 2).



131

132 **Figure 2:** Synthetic stratigraphic column of the middle Miocene-to-recent sedimentary interval (modified after Mancini et
 133 al., 2020).

134

135 The Laga Basin originated since the Messinian time (Ricci Lucchi, 1986; Roveri et al., 2002, 2003;
 136 Manzi et al., 2005; Bigi et al., 2006; Milli et al., 2007, 2009; Bigi et al., 2009; Cosentino et al.,
 137 2010) and evolved with the activation of major out-of-sequence thrust systems in the late
 138 Messinian-early Pliocene time (e.g., Billi & Tiberti, 2009) when, due to the compressional tectonic
 139 activity, the Laga Formation filled the confined foreland basin. Since the Pliocene time, the post-
 140 orogenic phase leads to the activation of the main extensional faults (e.g., Malinverno & Ryan,
 141 1986; Cavinato & De Celles, 1999) and the formation of fault-bounded intra-mountain basins that
 142 disarticulate the old orogenic framework (e.g., Cavinato, et al., 2002; Giaccio et al., 2012; Mancini
 143 et al., 2012; Pucci et al., 2015; Nocentini et al., 2017).

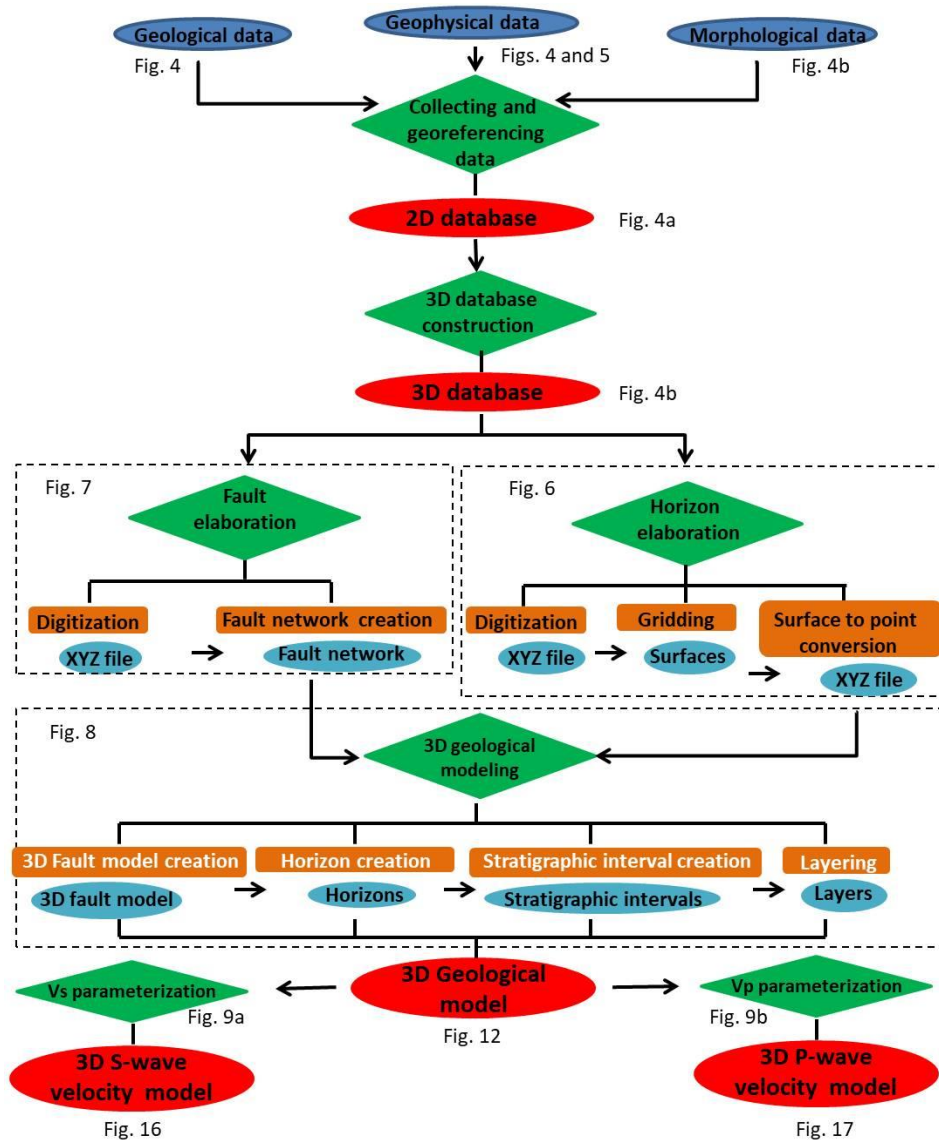
144 Today, this portion of central Apennines, where the study area is located, is a high-hazard region
 145 affected by post-orogenic extension occurring along Quaternary normal faults (e.g., Cavinato and
 146 De Celles, 1999; Galadini, 1999; Galadini & Galli, 2003, Mancini et al. 2019, Vignaroli et al.,
 147 2019; 2020; and reference therein) and causing widespread historical and instrumental seismicity
 148 (CSI, Castello et al., 2006; ISIDe working group, 2007; CPTI15 V2.0, Rovida et al., 2019; 2020)
 149 (Fig. 1).

150 The 2016-2017 seismic sequence in the Amatrice area consisted of many earthquakes aligned along
151 an NNW-SSE-trending, 60 km-long normal fault system (e.g., Scognamiglio et al., 2016;
152 Chiaraluce et al., 2017; Improta et al., 2019; Michele et al., 2020; and references therein). The
153 seismic sequence was characterized by three mainshocks: Mw 6.0 (on 24th August) located near the
154 Amatrice town; Mw 5.9 (on 26th October) at the northernmost border of the sequence, near the
155 Visso town; Mw 6.5 (on 30th October) that occurred right in the middle of the fault system already
156 activated in August, near the Norcia town (Fig. 1). In the same area, another catastrophic and
157 remarkably similar seismic event occurred in 1639, with an estimated Mw 6.2 mainshock (Tiberi
158 Romano, 1639; Rovida et al., 2019; 2020). Galli et al. (2016) suggest that the 1639 seismic event
159 could have been generated by the same seismogenic fault that ruptured in 2016. In the past, the
160 Amatrice and surrounding areas have been struck by other moderate-to-large seismic sequences, as
161 the 1703 L'Aquila (estimated Mw 6.7 mainshock; Rovida et al., 2019; 2020), the 1997 Colfiorito
162 (Mw 6.0 mainshock; Deschamps et al., 2000; Ripepe et al., 2000), and the 2009 L'Aquila (Mw 6.3
163 mainshock; Scognamiglio et al., 2010; Lucente et al., 2010; Chiaraluce et al., 2011; Herrmann et al.,
164 2011; Valoroso et al., 2013; Lavecchia et al., 2017) sequences. Like the 2016-2017 sequence, the
165 1997 Colfiorito and the 2009 L'Aquila sequences were characterized by the occurrence of multiple
166 events that activated 5-15 km long, southwest-dipping normal fault segments (Chiaraluce et al.,
167 2017).

168

169 **3 Data and methods**

170 This work is based on a multidisciplinary approach that integrates geological and geophysical
171 datasets (Fig. 3).



172
 173 **Figure 3:** Workflow chart. Main processes (green diamonds) and their sub-processes (brown rectangles), primitive (blue
 174 ellipses) and derived (light blue ellipses) data, realized databases and models (red ellipses) are represented. The
 175 contextualization of some figures in this paper is indicated.

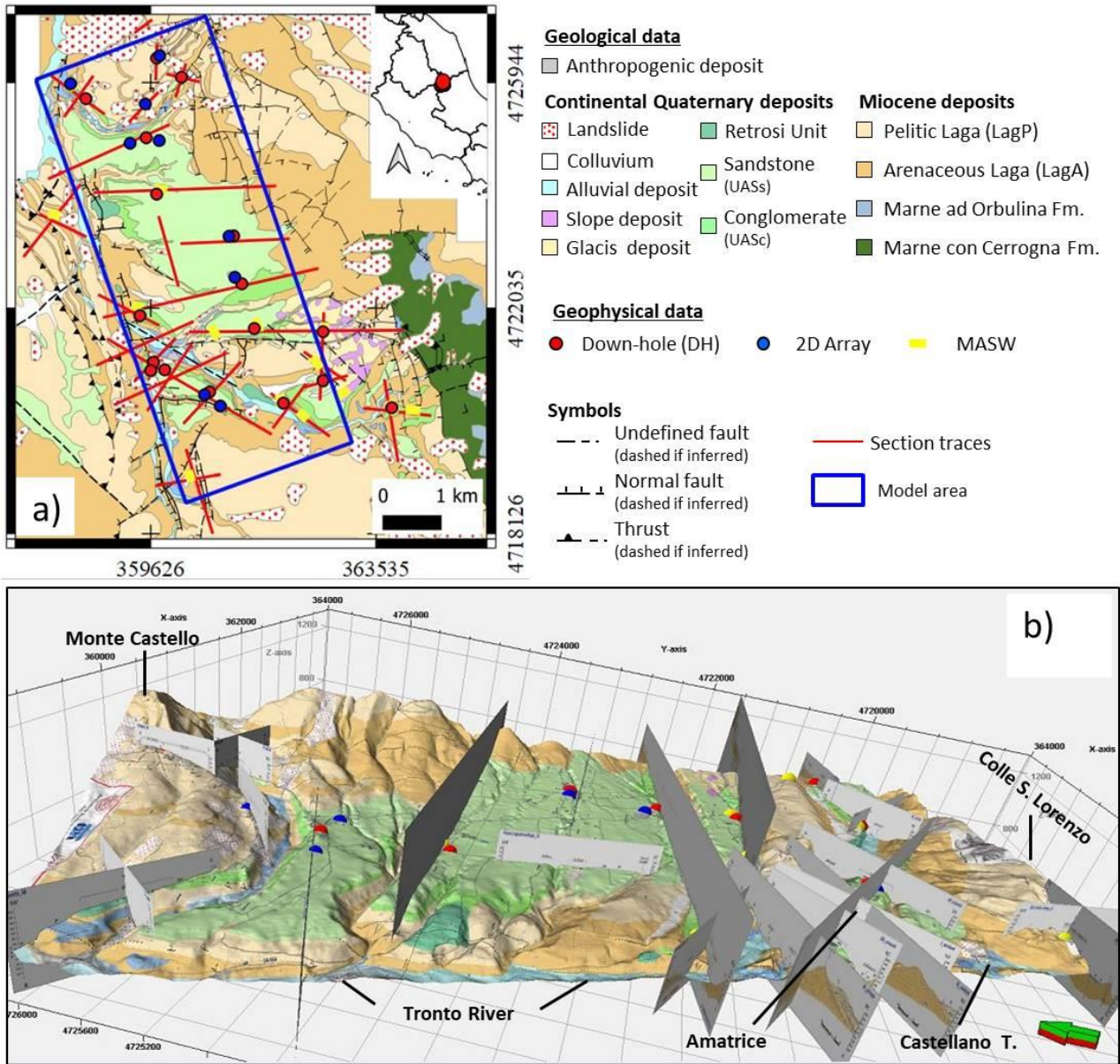
176
 177 **3.1 Data collection**

178 Geological and geophysical data derive from fieldworks and surveys performed at 1:5.000 scale and
 179 from published works on the area struck by 2016-2017 seismic sequence (Chiaretti & Nibbi, 2018;
 180 EmerTer Project Working Group, 2018; Milana et al., 2019; Vignaroli et al., 2019; 2020; Mancini
 181 et al., 2020; Del Gaudio et al., 2021). This geological dataset provides information on (i) nature,
 182 thickness and distribution of the main lithotypes, and (ii) orientation, geometry and kinematics of
 183 the main tectonic structures (e.g., faults and their associated fracture network). Surface geological
 184 data have been integrated with data from 16 Down-Hole (DH) measurements, 8 associated
 185 Multichannel Analyses of Surface Waves (MASW), to some of which (i.e., Cascello, Colloceta,
 186 Prato MASW) V_p values deriving from some seismic refraction profiles acquired along the same

187 traces have been associated, and 15 Horizontal-to-Vertical Spectral Ratio analyses (HVSr or 2D
 188 array). DHs reach a maximum depth of about 50 meters, while MASWs and 2D arrays in some
 189 cases exceed 200 meters in depth (Table 1), allowing to constrain the deeper parts of the
 190 geophysical model.

191 A 5 m-resolution digital elevation model (DEM), deriving from the 1:5.000-scale Regional
 192 Technical Map of the Rieti Province has been used as topographic base (Fig. 4).

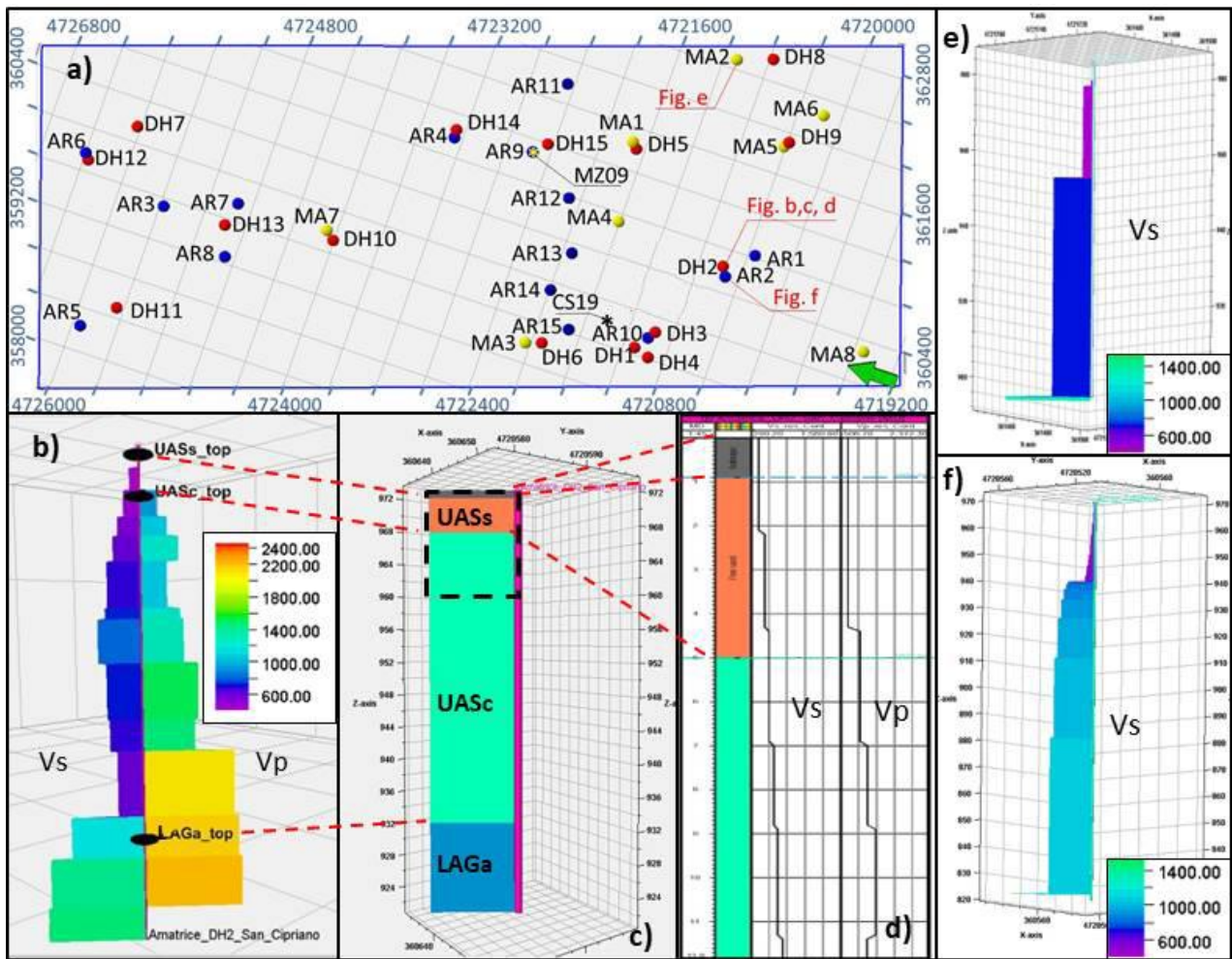
193



194
 195 **Figure 4:** Used data. (a) 2D GIS image of geological (geological map and cross-sections by Vignaroli et al., 2019) and
 196 geophysical data (general geological framework in figure 1); (b) 3D view of geological and geophysical data in the model
 197 area (blue rectangle in figure 1). The geological map is projected on a 5-m resolution Digital Elevation Model. The
 198 overlapped points represent the DH (red points), 2D array (blue points), and MASW (yellow points) locations. See figure
 199 3 to contextualize figures in the workflow.

200

201 DH data provided stratigraphic information, like lithofacies tops (classified according to Mancini et
 202 al., 2020, for the Quaternary deposits, and Vignaroli et al., 2019, for the Messinian Laga Formation)
 203 and velocity information (i.e., V_s and V_p velocities) of the drilled deposits (Figs. 5b, 5c, 5d).
 204 Finally, MASW (Fig. 5e) and 2D array (Fig. 5f) data have been used for constraining the wave
 205 velocities for each lithofacies (Table 1).
 206



207
 208 **Figure 5:** Subsoil geological and geophysical data. (a) Location map of seismic stations (black and yellow asterisks) and
 209 DH (red points), 2D array (blue points) and MASW (yellow points) measurement points; a code is associated with each
 210 measurement point (see corresponding extended names in table 1); the green arrow points north. (b) Lithofacies tops
 211 (black ellipses: UASs, Quaternary sandstones; UASc, Quaternary conglomerates; LAGa, arenaceous Laga) and velocity
 212 data (V_p and V_s) in the Amatrice-San Cipriano DH, also named Amatrice DH2; (c) lithofacies in the Amatrice-San Cipriano
 213 DH (grey, anthropic; orange, fine sand; light blue, gravel and sand; blue, sandstone and siltstone); (d) well section
 214 window of a portion of the Amatrice-San Cipriano DH; (e) V_s velocities of the Cascello MASW; (f) V_s velocities of the
 215 Amatrice 2D array. Seismic velocity values shown in color scales are expressed in m/s. A detailed list of used
 216 geophysical data is shown in table 1.
 217
 218

	NAME	CODE	Vs	Vp	LITHOFACIES	DEPTH (m)
DOWN-HOLE (DH)	Amatrice_DH1	DH1	×	×	✓	50
	Amatrice DH2-San Cipriano	DH2	✓	✓	✓	51
	Amatrice_DH3	DH3	✓	✓	✓	52
	Amatrice_DH4-San Francesco	DH4	✓	✓	✓	37
	Cascello_DH1	DH5	✓	✓	✓	50
	Cornillo_Vecchio_DH1	DH6	✓	✓	✓	20
	Cossito_DH1	DH7	✓	✓	✓	30
	Moletano_DH1	DH8	✓	✓	✓	31
	Retrosi_DH1	DH9	✓	✓	✓	50
	Rocchetta_DH1	DH10	✓	✓	✓	50
	Saletta_DH1	DH11	✓	✓	✓	30
	San_Capone_DH1	DH12	✓	✓	✓	30
	San_Lorenzo_Flaviano_Rio_DH1	DH13	✓	✓	✓	30
	Sant_Angelo_DH1	DH14	✓	✓	✓	40
	Sommati_DH1	DH15	✓	✓	✓	40
MASW	Cascello	MA1	✓	✓	×	100
	Collecreta	MA2	✓	✓	×	30
	Cornillo_Vecchio	MA3	✓	×	×	30
	Prato	MA4	✓	✓	×	90
	Retrosi1	MA5	✓	×	×	30
	Retrosi2	MA6	✓	×	×	40
	Rocchetta	MA7	✓	×	×	35
	S.Lorenzo_Pinaco	MA8	✓	×	×	30
2D ARRAY	AMA03	AR1	✓	×	×	30
	Amatrice	AR2	✓	×	×	150
	CAS08	AR3	✓	×	×	120
	S.Angelo	AR4	✓	✓	×	199
	SAL04	AR5	✓	×	×	37
	SCP01	AR6	✓	×	×	80
	SLO01	AR7	✓	×	×	197
	SLO02	AR8	✓	×	×	35
	Sommati	AR9	✓	✓	×	195
	Milana et al., 2019	AR10	✓	×	×	150
	Sommati transect (point S05)	AR11	✓	×	×	312
	Sommati transect (point S06)	AR12	✓	×	×	259
	Sommati transect (point S07)	AR13	✓	×	×	265
	Sommati transect (point S08)	AR14	✓	×	×	248
	Sommati transect (point S09)	AR15	✓	×	×	208

220

221

222

223

224

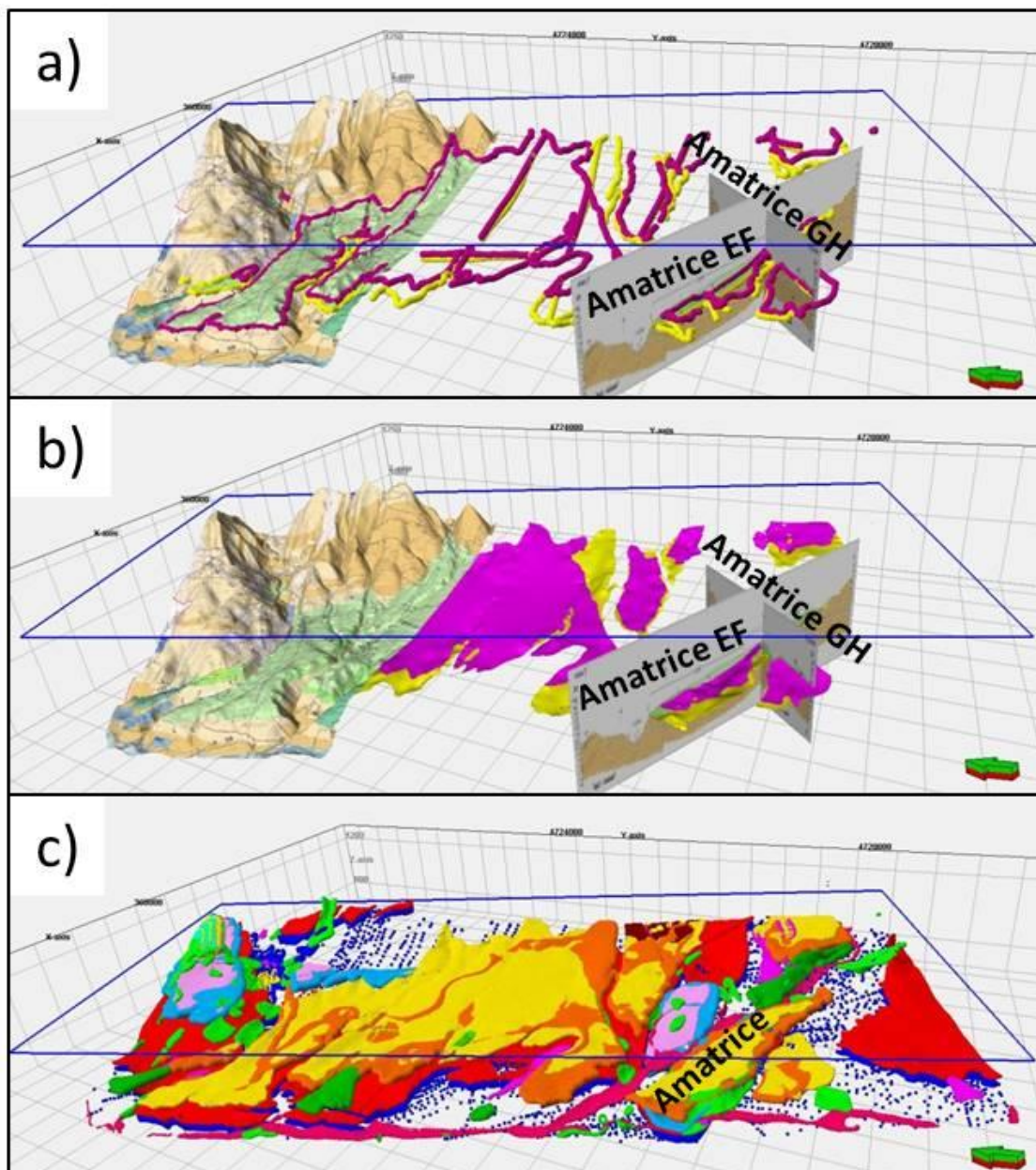
225

Table 1: List of used subsoil geological and geophysical data. The extended names and codes of measurement points are reported respectively in the “name” and “code” columns, while the availability of geological and geophysical data is indicated in “Vs”, “Vp”, and “lithofacies” columns (green checks, available data; red crosses, not available data). In the “depth” column the maximum investigation depths are expressed in meters from the ground surface. Locations of the measurement points in figure 5a.

226 3.2 Data preparation and 3D modeling

227 Geological and geophysical data have been firstly homogenized in terms geological coding (i.e.,
228 stratigraphy and lithofacies), quality checked and geo-referenced to a common Spatial Reference by
229 using a GIS software (Fig. 4a), and finally uploaded into a 3D geological and geophysical modeling
230 software (Fig. 4b).

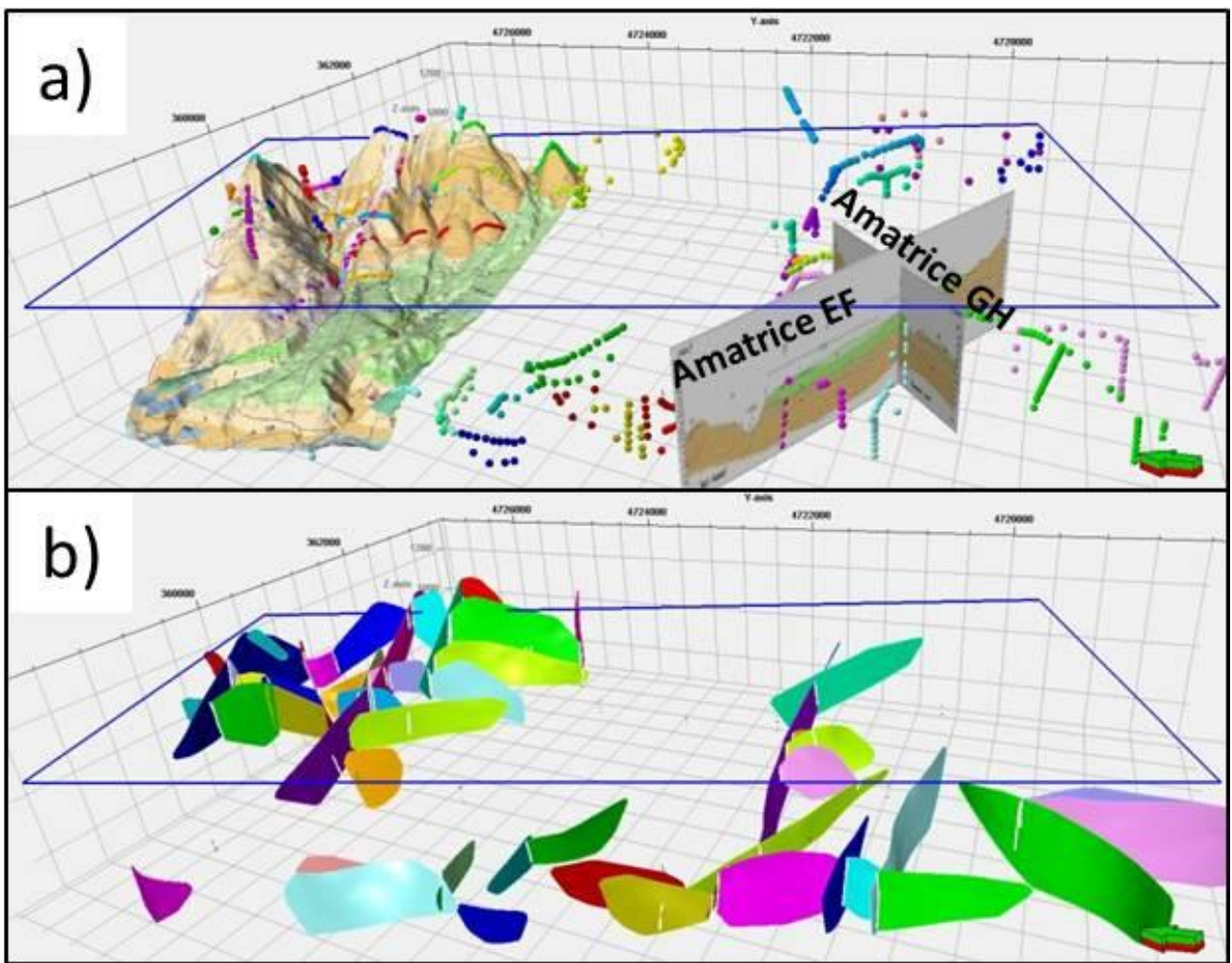
231 Firstly, all stratigraphic boundaries (lithofacies surfaces) have been digitized on the geological map
232 and cross-sections (Fig. 6a). Then, the XYZ point file obtained for the digitized horizons, integrated
233 with the lithostratigraphic tops intercepted in core-wells, have been gridded. Lithofacies surfaces
234 have been so created (Fig. 6b), manually edited where required, and finally converted back into
235 XYZ point files. In this way, we obtained denser XYZ point files (Fig. 6c) to better constrain the
236 construction of horizons during the 3D modeling phase (see Figure 3).



237

238 **Figure 6:** Horizon elaboration workflow. 3D view of digitized horizons: (a) bases of Quaternary sandstones (UASs)
239 (purple points) and conglomerates (UASc) (yellow points) digitized on geological map and cross-sections; (b) gridded
240 surfaces of the UASs and UASc bases; (c) all digitized horizon (XYZ points). Figures a and b show the northern portion
241 of the geological map; two representative geological cross-sections (named Amatrice AB and Amatrice GH) are also
242 reported for illustrating the spatial correlation of the data. See figure 3 to contextualize figures in the workflow.
243

244 Faults have been digitized on the geological map and cross-sections (Fig. 7a). The resulting XYZ
245 point files have been finally used as input data to create the fault network (Figs. 3 and 7). It defines
246 faults in the geological model that represents the basis for the development of 3D meshes. The
247 generated faults, in fact, define breaks in the grid, along which the digitized stratigraphic horizons
248 should be offset.



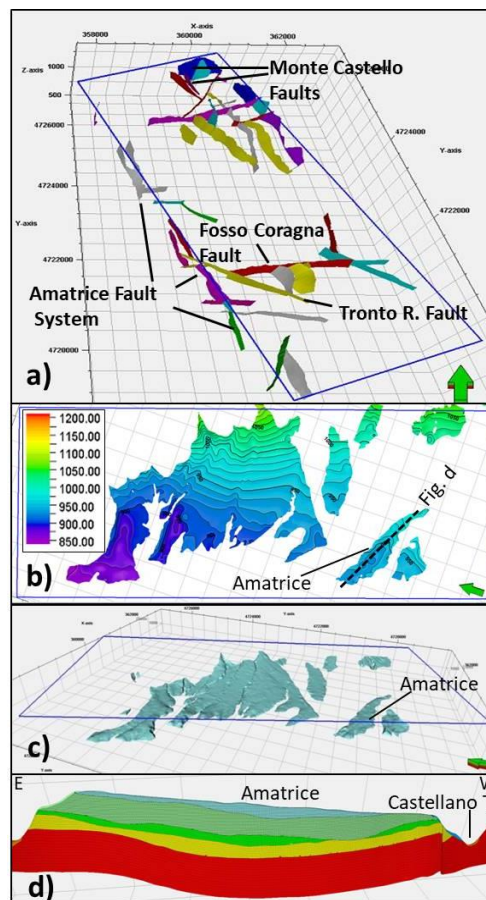
249 **Figure 7:** Fault elaboration workflow. (a) 3D view of faults digitized on geological map and cross-sections (XYZ points);
250 (b) 3D view of the processed fault network (solid colored surfaces). In figure the northern portion of the geological map
251 and two representative geological cross-sections (named Amatrice AB and Amatrice GH) are also reported for illustrating
252 the spatial correlation of the data. See figure 3 to contextualize figures in the workflow.
253

254
255
256 The resulting stratigraphic horizons and faults have been finally checked and, if necessary,
257 corrected to obtain the best fit between their geometry and their outcroppings. Eventually, they have

258 been hierarchized according to the stratigraphic position (for horizons) and cross-cutting
259 relationships (for faults).

260 The final 3D geological model has been generated with the following procedure. First, the created
261 fault network has been incorporated into a 3D mesh (Fig. 8a), whose average areal resolution has
262 been set to 5 meters. Then, the horizons (Fig. 8b) and the included stratigraphic intervals (Fig. 8c),
263 have been reconstructed. Finally, the resulting stratigraphic intervals have been divided into layers
264 (Fig. 8d).

265



266

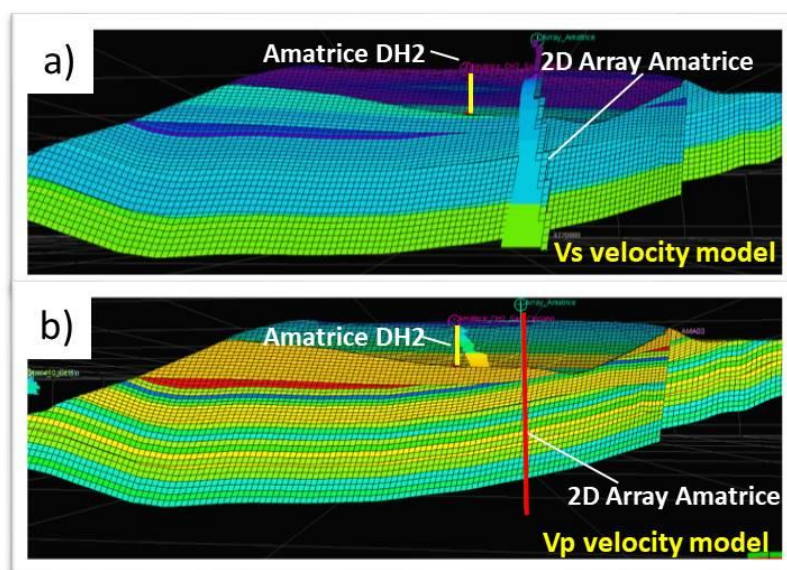
267 **Figure 8:** 3D modeling workflow. (a) Fault network generation; (b) Horizon creation (in the figure is shown the contour
268 line map of the base of Quaternary sands); (c) stratigraphic interval creation (in the figure is shown the created
269 Quaternary sandstone zone); (d) layering. See figure 3 to contextualize figures in the workflow.

270

271

272 The 3D geological model has been finally parameterized with the V_s and V_p velocities derived by
273 the DH, MASW (with the associated seismic refraction profiles where available), and 2D array
274 measurements (Fig. 5; Tab. 1). First, we have parameterized the 3D model cells located along the
275 DH, MASW (or seismic refraction profiles for V_p data), and 2D array paths by running a “well log
276 upscaling” process, then, starting from the upscaled cells, the entire 3D model has been populated
277 with the V_s and V_p data following the geological model layering (Fig. 9). In this way, two

278 preliminary geology-based 3D velocity models have been constructed (Figs. 16 and 17). The
 279 parameterization of the 3D geological model has been carried out by using a “moving average”
 280 interpolation algorithm by Petrel software. The “moving average” algorithm calculates averaged
 281 values for cells starting from the input data, to which a weight is associated as a function of the
 282 distance from the measurement points. The algorithm is fast and does not generate smaller or bigger
 283 values than the minimum and maximum velocity values of the upscaled cells. Furthermore, the
 284 "moving average" algorithm, considers the effects of structural (e.g., fault network) and
 285 sedimentary (e.g., lithology and anisotropy) conditions on the spatial distribution of geophysical
 286 attributes (Shao et al., 2012; Grunis & Khasanov, 2017).



287
 288 **Figure 9:** Model parameterization with Vs (a) and Vp (b) values. (a) A section of the Vs velocity model through the
 289 Amatrice plateau with the Amatrice DH2 down-hole (on the section) and the Amatrice 2D array (projected) Vs data; (b) a
 290 section of the Vp velocity model through the Amatrice plateau with the Amatrice DH2 down-hole (on the section) Vp data.
 291 On the two models the 3D geological model layers and cells can be observed. See figure 3 to contextualize figures in the
 292 workflow.

293
 294 A preliminary calibration of the realized 3D model has been done by processing the ellipticity
 295 curves (see Fäh et al., 2001) of the Rayleigh fundamental mode at two selected sites (hereafter
 296 control points).

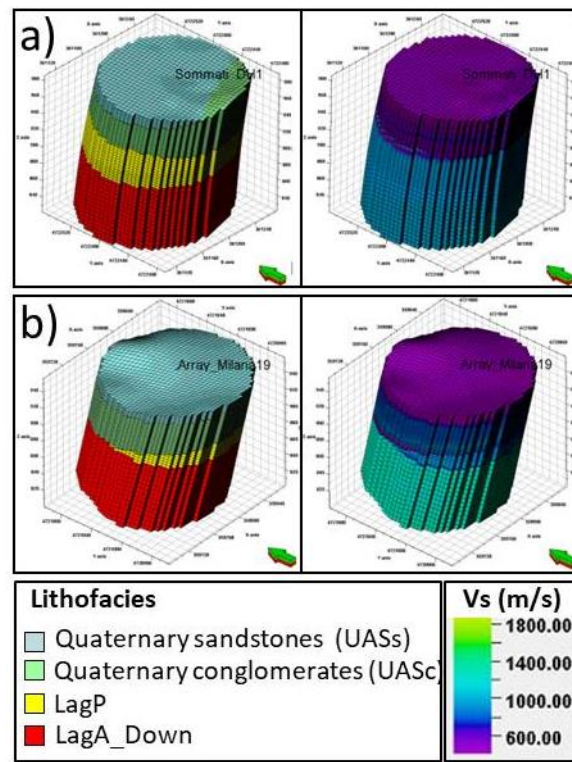
297 The procedure of calibration consists of three steps:

- 298 1. around each control point, cylindrical 3D meshes (with a radius of 75 m) are extracted (Fig.
 299 10);
- 300 2. meshes are organized in seismo-stratigraphy profiles in order to define, for each layer, the
 301 thickness in meters, the unit weight in Kg/m^3 , the V_p and V_s velocity models in m/s;

302 3. ellipticity curves of the Rayleigh fundamental mode are computed through the open-source
303 software Geopsy (<http://www.geopsy.org/>) and compared with the available HVSR curves
304 (Fig. 11).

305 The selected control points are in the northeastern part of the Amatrice town (i.e., Amatrice
306 historical center, in correspondence of the Milana et al., 2019 2D array), seriously damaged during
307 the 2016-2017 seismic sequence, and in correspondence of the Sommati DH1 site (Fig. 10). This
308 selection was made to focus the attention on some points where the evidence of 2D\3D effects has
309 been demonstrated (Gaudioiosi et al., 2021).

310



311

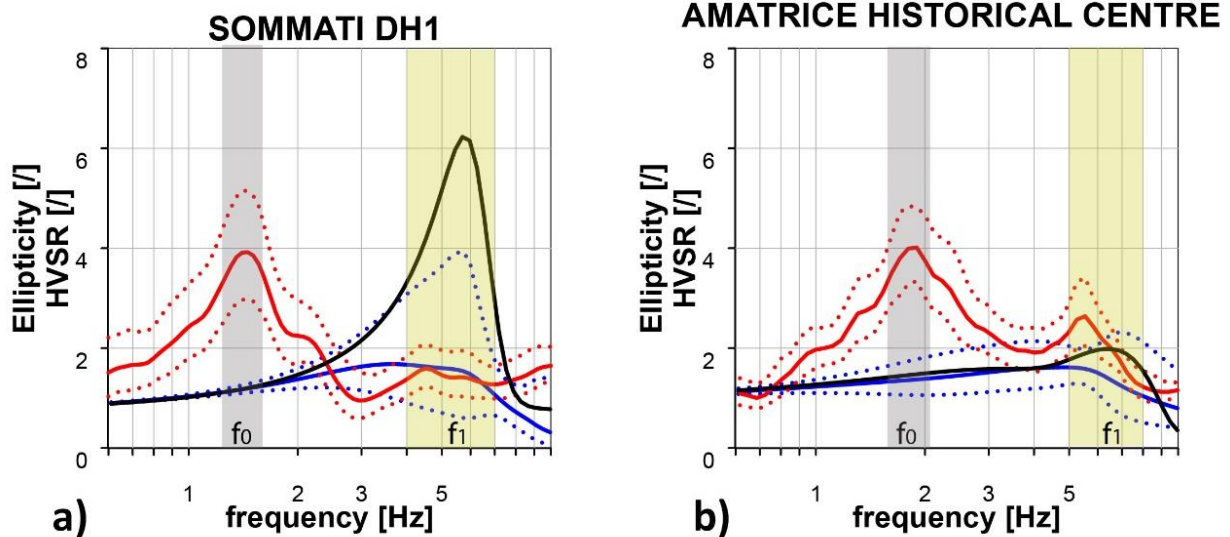
312 **Figure 10:** Extracted 3D geological (left) and Vs velocity (right) meshes. The cylindrical meshes (75 m radius) are
313 centered on the Sommati DH1 (a) and Amatrice historical center (in correspondence of the Milana et al., 2019 2D array)
314 (b). Green arrow points north. Site locations are reported in Figure 5a.

315

316 The HVSR curves have been automatically scanned to identify the frequencies f at which the
317 maximum amplitudes occur. In this study, the frequency value f_0 is assigned to the lowest
318 fundamental peak of frequency determined for each HVSR curve in the range 1-10 Hz. The f_0
319 frequency and its standard deviation (according to the SESAME criteria; SESAME, 2004) have
320 been plotted in Fig. 11.

321

322



323

324

325

326

327

328

329

330

331

332

333

334

335

Figure 11: Comparison between ellipticity (blue and black lines) and experimental HVSR curves (red lines) at the chosen control points. The figure shows the comparison of the ellipticity curves at (a) Sommati DH1 and (b) Amatrice historical centre (in correspondence of the Milana et al., 2019 2D array) sites with the experimental HVSR curves recorded at the nearest seismic stations: MZ09 for Sommati DH1 site and CS19 for Amatrice historical centre site. Ellipticity curves are represented considering both the response for the entire cylindrical mesh (blue curves), and a singular vertical profile at its center (black curves). Standard deviations of ellipticity and experimental HVSR curves (dashed blue and red lines, respectively) have been also considered. The grey vertical bands represent the f_0 frequency and its standard deviation computed over all the curves from time windows of 50 s length (according to the SESAME criteria; SESAME, 2004). The yellow vertical bands represent the highest amplified frequency band (f_1). The related 3D geological and V_s velocity meshes are shown in figure 10. Locations of the chosen control points and seismic stations are shown in figure 5a.

335

4 Results

336

337

338

This work provides two georeferenced databases (i.e., a 2D GIS and a 3D databases), a high-resolution 3D geological model, and two preliminary geology-based 3D velocity models (i.e. V_s and V_p velocity models) of the Amatrice Basin.

339

4.1 Georeferenced databases

340

341

342

343

344

345

346

347

Both georeferenced databases (i.e., 2D and 3D) share a common Spatial Reference System (see the appendix section) and classify the data according to their data type (e.g., topography data, geological section, maps, geophysical data, wells, horizons, faults, etc.). The GIS database consists of a 2D georeferenced database that collects morphological (topography contour lines), geological (sections and fault traces, maps, etc.), geophysical (seismic line and MASW traces, HVSR and DH position, etc.), and seismological (epicentral locations of the seismicity of the area) data. The data are subdivided into images (e.g., maps) and vectorial data (i.e., shapefiles). The latter are, in turn, grouped into points, lines, and polygons.

348 The 3D database contains the previous data that are combined with the related depth information.
349 3D data can be subdivided into two main groups: primitive data, which consist of the collected data
350 (i.e., well positions, geological cross-sections and maps, velocity data, etc.), and derived data, which
351 consist of the data produced during the various processing phases (i.e., digitized horizons and faults,
352 lithostratigraphic and fault surfaces, etc.) for constructing the 3D geological model.

353 *4.2 The 3D geological model*

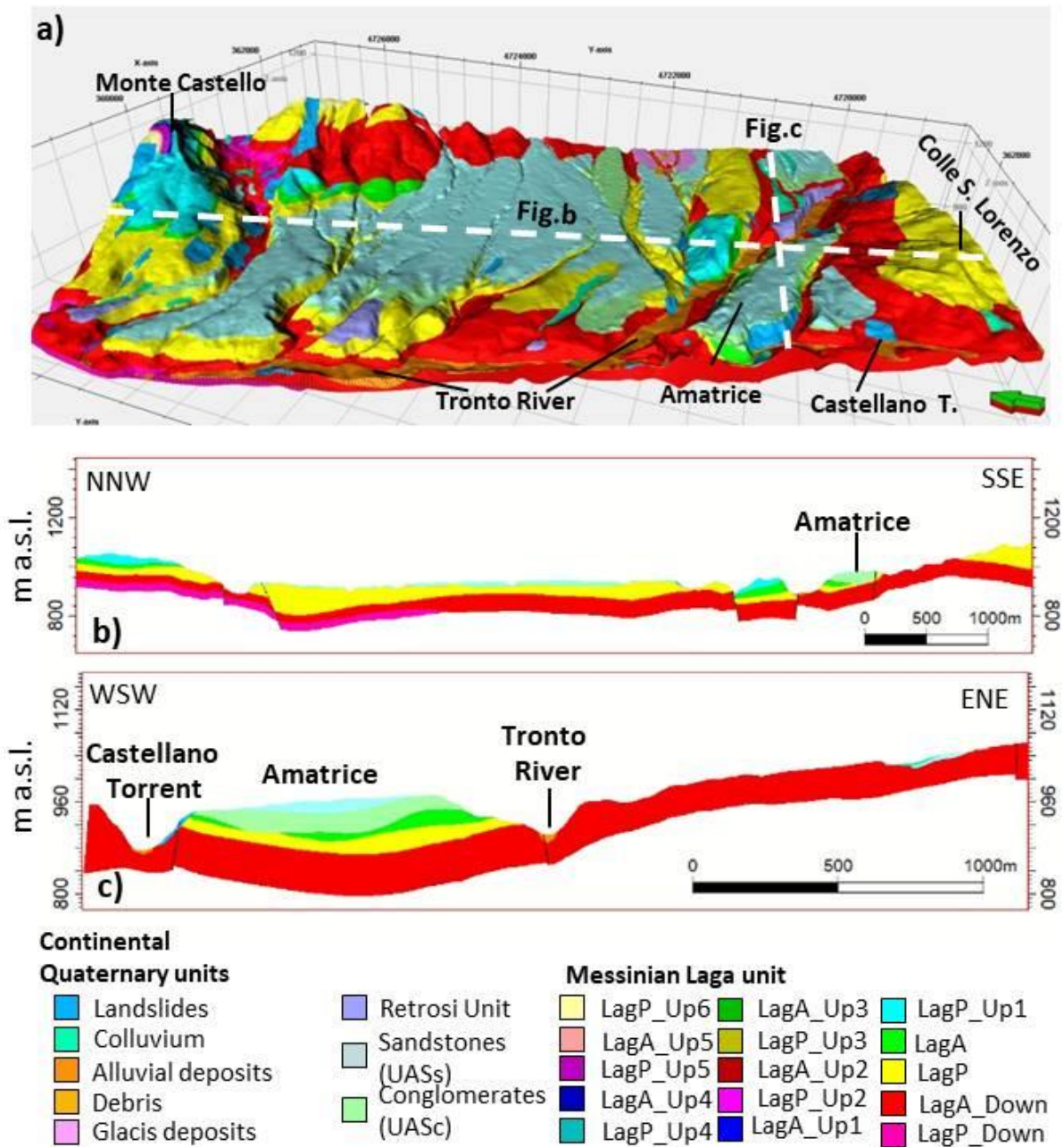
354 The performed 3D geological model covers an area of about 24.7 km² and extends about 200 meters
355 deep from the topographic surface, with local variations. The area, elongated in NNE-SSW
356 direction, is about 7.8 km long and 3.2 km wide, and extends from Monte Castello to Colle San
357 Lorenzo hamlets, 1.5 km south-east of the Amatrice hamlet (Figs. 4 and 12a). Its western edge
358 roughly follows the orientation of the Tronto River up to the Cornillo Vecchio village and then,
359 southward, follows the Castellano Torrent.

360 The areal size of cells is 5 meter in the whole area, while the vertical thickness of cells varies from
361 1 meter for the Quaternary interval, where more data are available and a higher resolution is
362 required, to 3 or 5 meters for the Messinian turbiditic interval (Fig. 8d).

363 The DEM represents the top surface of the model. From top to bottom, two main stratigraphic
364 successions can be distinguished: the Quaternary continental deposits and the underlying Messinian
365 Laga Formation. The surfaces that delimit the Quaternary continental deposits are erosive, while the
366 underlying ones are conformal (i.e., non-erosive stratigraphic surfaces). The latter represent the
367 interfaces bounding the arenaceous and pelitic intercalations of the Laga Formation.

368 Quaternary deposits are discontinuously distributed, thus forming isolated patches in the model. On
369 the other hand, the Laga Formation can be traced continuously through the whole studied area. The
370 modeled faults consist of normal faults, which mainly affect the Laga Formation and are generally
371 sutured by the Quaternary deposits, except for rare and limited exposures (Fig. 12).

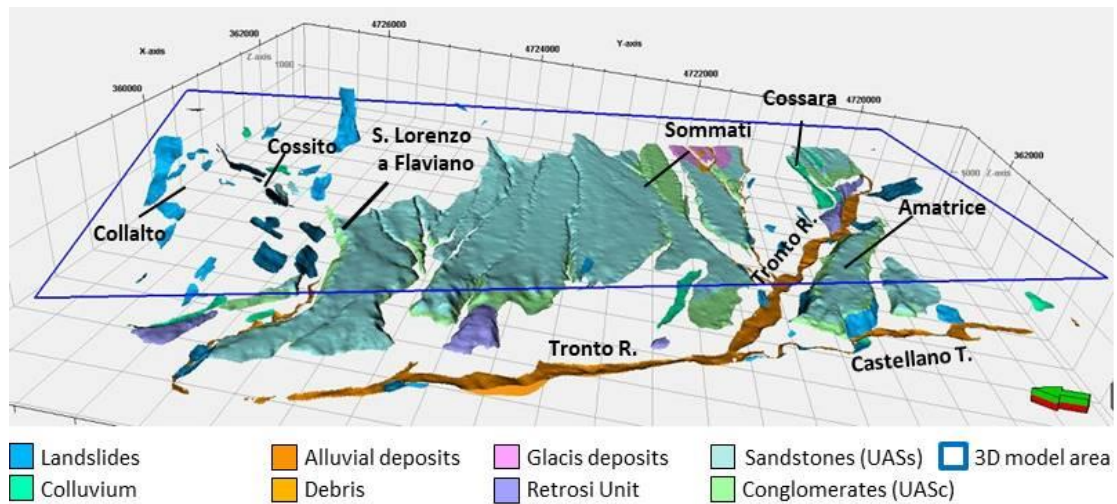
372



373
 374 **Figure 12:** 3D geological model of the study area. (a) View of the 3D geological model; (b) NNW-SSE and (c) WSW-ESE
 375 cross-sections through the model (traces in a). Green arrow points north. See figure 3 to contextualize this figure in the
 376 workflow.
 377

378 4.2.1 Quaternary units

379
 380 The following deposits were modeled for the Quaternary succession: landslide bodies; colluvium;
 381 debris; fluvial (e.g., Retrosi Unit) and recent alluvial deposits; Quaternary sandstones and
 382 conglomerates (Fig. 13).



383

384 **Figure 13:** Modeled Quaternary deposits. In this figure a 3D view of the modeled Quaternary deposits is shown. Blue
 385 rectangle delimits the modeled area. Green arrow points north.

386

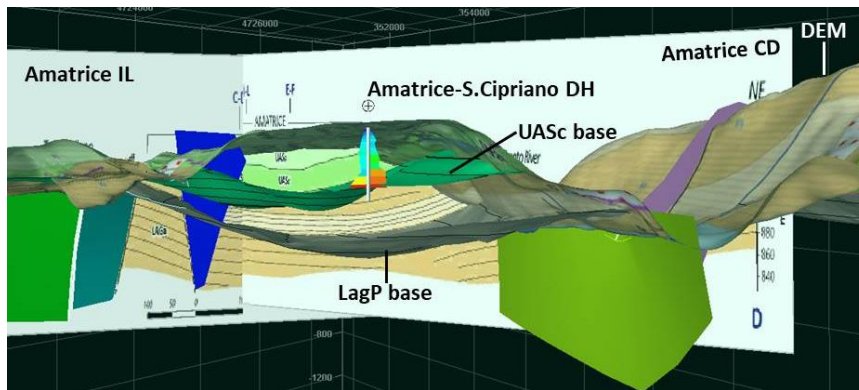
387 The landslide bodies, alluvial deposits, sandstones, and conglomerates represent the most
 388 widespread Quaternary deposits in the area.

389 Landslides overlap both the Quaternary and Messinian successions. Their thickness, unraveled by
 390 the interpretation of the geological cross-sections, ranges from less than one meter to a few meters.
 391 Small to moderate size landslides (~ 0.01 to 0.2 km^2) located at higher altitudes were mapped in the
 392 northern portion of the modeled area (surrounding areas of Casale, Collalto, and Cossito hamlets)
 393 and in the southern one (surrounding area of Amatrice hamlet). Two medium-sized landslides are
 394 located along the north-eastern ($\sim 0.03 \text{ km}^2$) and south-western ($\sim 0.06 \text{ km}^2$) slope of the
 395 northernmost portion of the Amatrice terrace. The landslide bodies in the middle area, between San
 396 Lorenzo a Flaviano and Sommati villages, are instead rare and small ($\leq 0.01 \text{ km}^2$).

397 Alluvial deposits are mainly made up of river deposits that fill the Tronto River and the Castellano
 398 Torrent riverbeds. They are located along the western edge of the model and immediately northeast
 399 of Amatrice village. Their thickness, defined by the geological sections, is up to a few meters,
 400 changing both along and across the riverbed.

401 Quaternary sands cover a large part of the model area. The most extensive outcrop ($\sim 5.6 \text{ km}^2$) is in
 402 the central area, where its base descends, as well as the slope, from northeast to southwest, towards
 403 the Tronto River (Fig. 8b). Other medium-sized (~ 0.2 to 0.5 km^2) outcrops are present in the
 404 Amatrice, Prato-Voceto, and Cossara areas. A limited number of small outcrops ($\leq 0.02 \text{ km}^2$) can
 405 also be observed in the model. This lithofacies overlaps in part the Quaternary conglomerates and in
 406 part the Messinian foredeep deposits. Its average thickness ranges from few meters to about 20-25
 407 meters. In the Amatrice village area, the base of the lithofacies shows an upward concave shape and
 408 reaches its maximum thickness (approx. 20 meters) in the middle part of the terrace.

409 The Quaternary conglomeratic lithofacies interposes between Quaternary sands and Messinian
 410 foredeep deposits. It is characterized by a variable thickness ranging from a few meters up to about
 411 30-35 meters. Its base is an erosive surface characterized by culminations and depressions. In the
 412 central area, this base shows a general dip from east to west, while in the Amatrice area it shows a
 413 general upward concave shape (Fig.14). Quaternary conglomerates and sands are characterized by
 414 mostly horizontal internal layering.



415
 416 **Figure 14:** 3D view of the Amatrice subsoil. The figure shows the processed UASc and LagP bases. The upward
 417 concave geometry of the stratigraphic horizons is evident. Two geological cross-sections (i.e., Amatrice CD and Amatrice
 418 IL), the Amatrice-San Cipriano DH (also named Amatrice DH2) and the associated S-wave (left) and P-wave (right)
 419 velocities, the DEM, and some processed faults (solid-colored vertical surfaces) are shown.

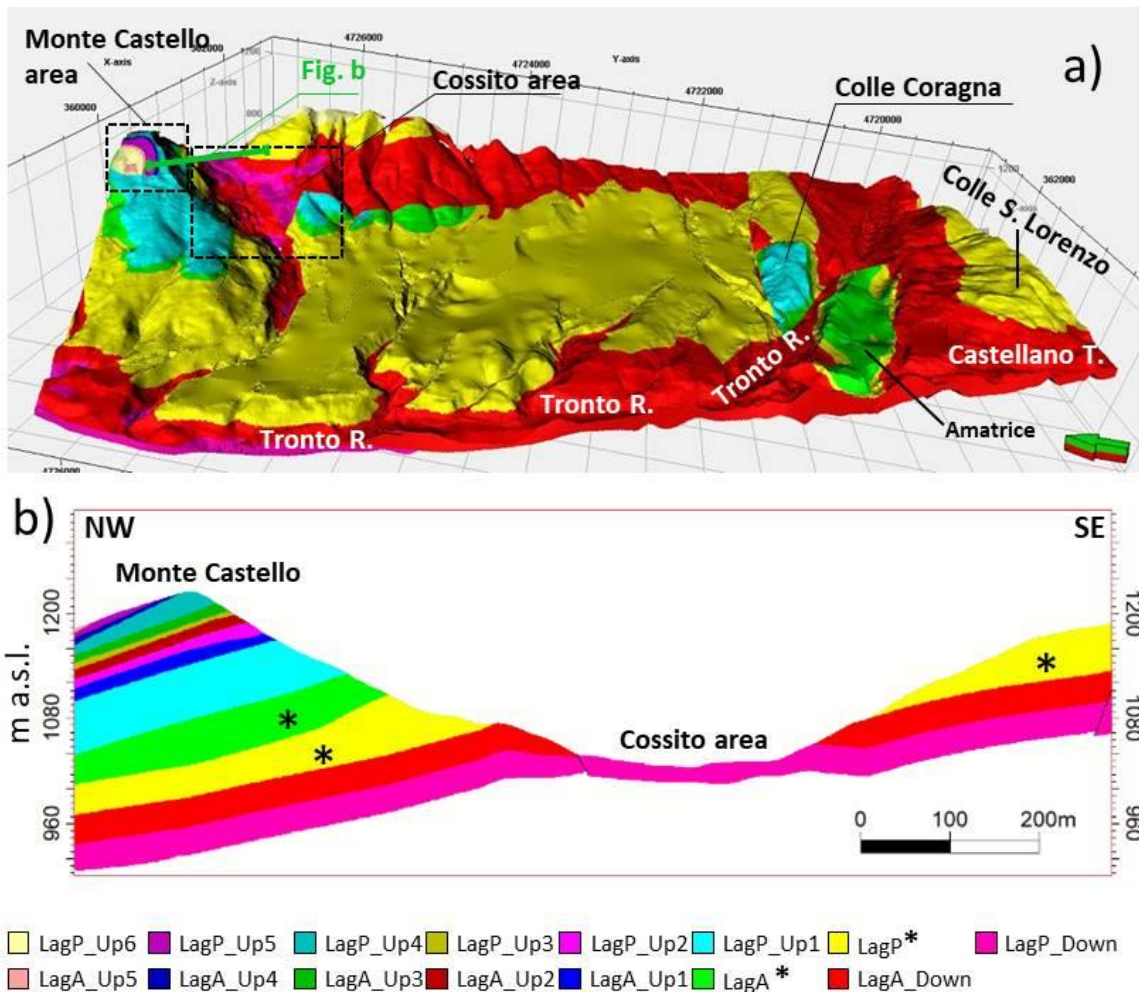
420

421 4.2.2 Messinian foredeep deposits

422

423 The Messinian foredeep deposits of the Laga Formation are made up of an interlayering between
 424 arenaceous and pelitic layers. Overall, we reconstructed eight pelitic lithofacies and seven
 425 arenaceous ones. Some arenaceous and pelitic intercalations (i.e., LagA and LagP) have been
 426 considered as reference horizons to hierarchize and denominate all the Laga intercalations. The
 427 name associated to each lithofacies contains both lithological (i.e., "A" for arenaceous and "P" for
 428 pelitic) and stratigraphical (i.e., "down" for layers below reference horizons and "up" for layers
 429 above reference horizons; numbers, proceeding upwards with respect to the reference horizons,
 430 indicate the stratigraphic position of the arenaceous and pelitic intercalations) information (Fig 15).

431



432
 433 **Figure 15:** Modeled Laga deposits. (a) 3D view of the modeled Laga deposits. The overlying Quaternary deposits have
 434 been switched off. Monte Castello and Cossito areas are shown (black dashed rectangles). Green arrow points north. (b)
 435 Geological cross-section across the Monte Castello and Cossito areas (trace in a; green line). In Monte Castello area an
 436 upward reduction of the intercalation thickness can be observed. Black asterisks indicate the reference horizons.
 437

438 The deepest Messinian horizon (i.e., LagA_Down base) and the underlying lithofacies (i.e.,
 439 LagP_Down layer), identified below the reference horizons, have been modeled exclusively on the
 440 basis of the data collected in the Cossito surrounding area, the only area where they crop out (Fig.
 441 15). The LagA layer (reference horizon) widely cropping out in the model area, while the overlying
 442 ones sporadically cropping out in some smaller areas (e.g., LagP layer, Amatrice and Monte
 443 Castello areas; LagP_Up1 layer, Colle Coragna and Monte Castello areas). The stratigraphically
 444 higher Laga portion (i.e., from LagA_Up1 to LagP_Up6 layers), instead, crops out exclusively in
 445 Monte Castello area, where layers have been lowered by normal faults bounding the Monte Castello
 446 structure. This interval consists of a rapid alternation of thin arenaceous and pelitic intercalations
 447 (Fig. 15).

448 In some cases, the thickness of Messinian lithofacies varies due to the original shape of the
 449 sedimentary basin and/or erosional phenomena.

450 Laga intercalations are overlaid by younger Messinian layers by means of conformal surfaces or by
451 Quaternary continental deposits by means of erosive surfaces.

452

453 4.2.3 Faults

454

455 The Messinian foredeep deposits appear disarticulated by an extensional fault system located at the
456 hanging wall of a major west-dipping normal fault (i.e., the Gorzano-Laga Fault), to which defines
457 a subsidiary structure (Vignaroli et al., 2020) (Fig. 1). Most of normal faults have been mapped in
458 the southwestern and northeastern portions of the 3D geological model, while the central part
459 (between Rocchetta and Sommati villages) lacks the occurrence of such tectonic structures.
460 However, we cannot exclude the presence of additional faults sealed by the Quaternary continental
461 deposits.

462 Two main fault trends can be identified: an NNW–SSE and an E-W one (Fig. 8a). When observed,
463 the E-W-striking system systematically cut and dislocates the NNW-SSE-striking one. Fault plains
464 are generally characterized by high dip angles ($>60^\circ$) and their length varies from a few hundred
465 meters up to a few kilometers.

466 The NNW-SSE striking normal fault system is observed along the western boundary of the model.
467 This fault system, named Amatrice Fault System, runs along the Tronto River in his northern
468 portion, up to the Cornillo Vecchio village, and along the Castellano Torrent in his southern
469 portion. This fault system is segmented into several portions by some small E-W normal faults (Fig.
470 8a).

471 Along some faults a rotational movement of the fault blocks around the intermediate stress axis (σ_2)
472 is observed (scissor faults). The rotation causes the block lifting on one side and its lowering on the
473 other side. In the Monte Castello area, for example, Messinian deposits are lowered northwestwards
474 and raised southeastwards by the activity of the faults bordering the Monte Castello structure, while,
475 in the Colle Coragna area, the Messinian deposits are lowered westwards and raised eastwards by
476 the activity of the Fosso Coragna and the Tronto River faults (Figure 8a). The rotation in both cases
477 gives to the Messinian deposits the aspect of monoclines with different dip with respect to the
478 surrounding deposits.

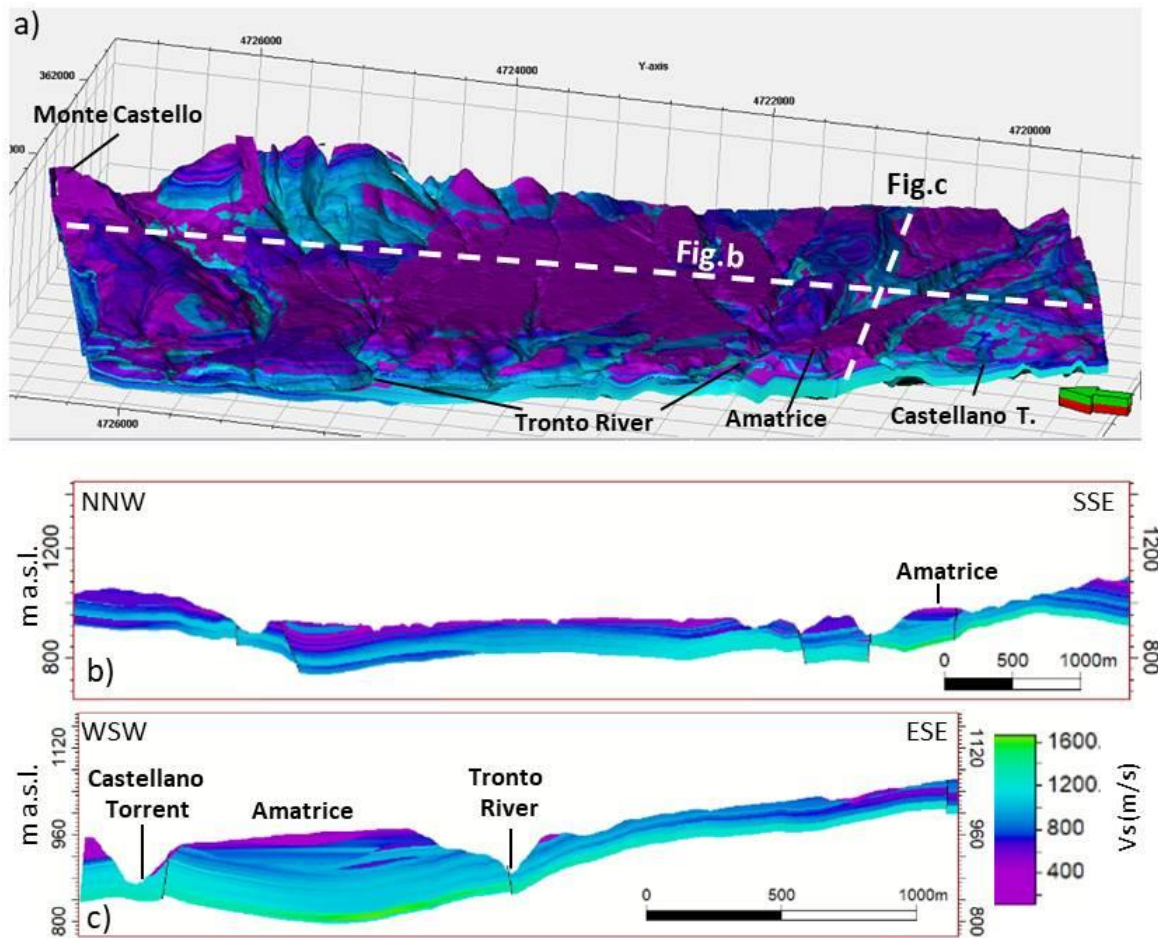
479

480 4.3 3D velocity models

481 The reconstructed geology-based V_s and V_p velocity models represent a first attempt to
482 parameterize the geological model, aimed at defining the 3D distribution of the geophysical
483 parameters in the modeled geological volume. Starting from the parameterized cells along the DH,
484 MASW (or seismic refraction profiles for V_p data), and 2D array measurement path (upscaled

485 cells), the V_s and V_p velocities populate the entire 3D model with a gradual value variation defined
486 by the adopted “moving average” algorithm following the geological model layering (Figs. 16 and
487 17).

488 The V_s model (Fig. 16) is characterized by velocity values that are in a range between 100 m/s (at
489 the top of the SLO01 2D array) and 1667 m/s (at the base of the Amatrice 2D array). They show a
490 general downward increasing, with marked local velocity inversions within the modeled succession.
491 The lowest V_s values (about 100 m/s) are observed in correspondence of the Quaternary continental
492 deposits. In some cases, a sudden increase in V_s values (from 607 m/s to 1170 m/s at 37.7 m depth
493 of the Amatrice DH2-San Cipriano Down-Hole, 2.3 meters above the Quaternary base) occurs near
494 the transition between Quaternary deposits and Messinian foredeep deposits (Figs. 9a, 16b and 16c).
495 The V_s values of the Messinian foredeep deposits vary from a few hundred meters per second up to
496 a maximum of 1667 m/s near the model base, as also recorded at the bottom of the Amatrice 2D
497 array. Within the Messinian succession there are some local velocity inversions, which are likely
498 due to the lithological interlayering of the arenaceous-pelitic succession. Low velocity values are
499 sometimes observed within the uppermost (few meters) layers of the Laga lithofacies (e.g., at the
500 top of the San Capone DH1, $V_s = 162$ m/s) and interpreted as the effect of weathering.



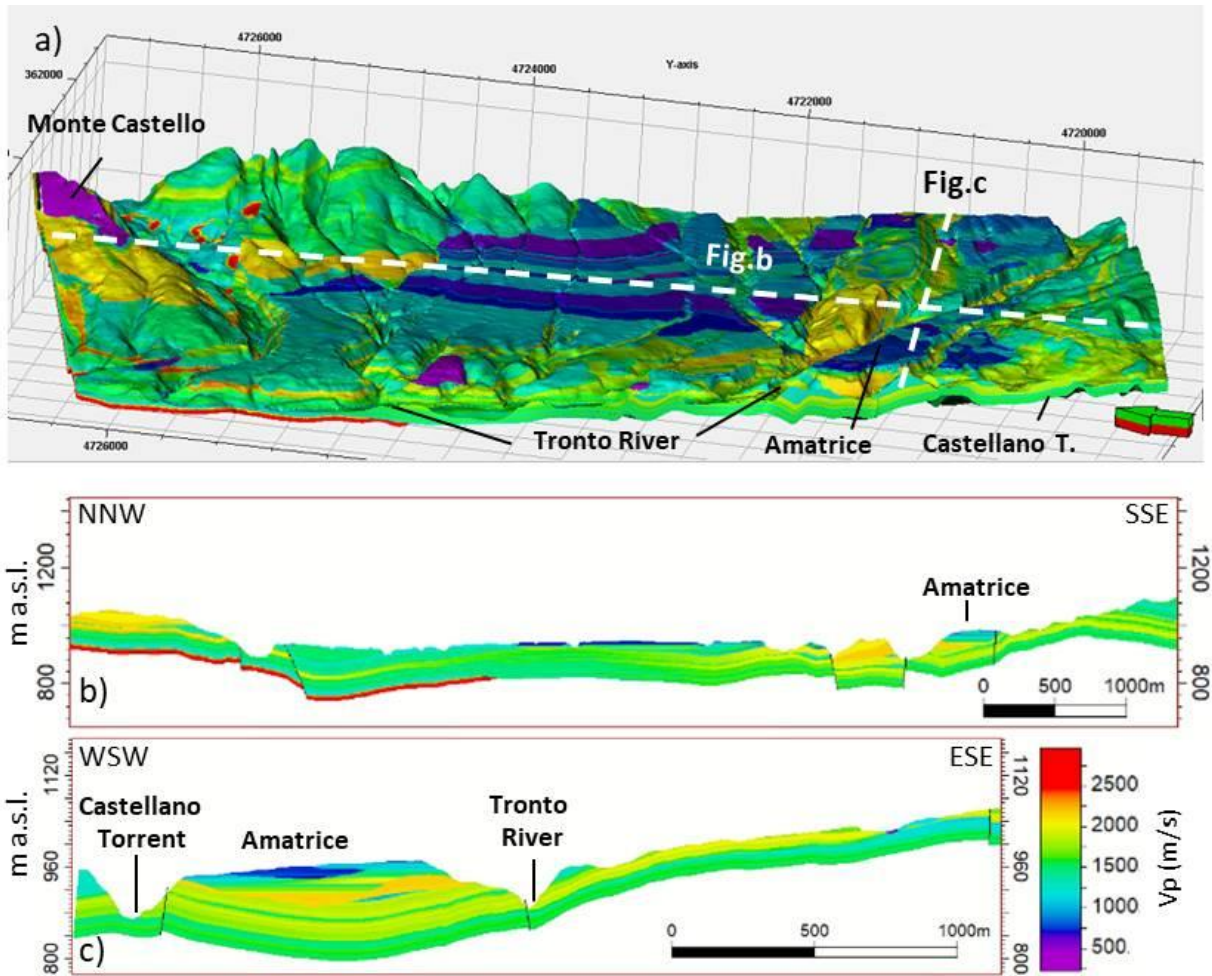
501

502 **Figure 16:** 3D V_s velocity model. (a) View of the 3D V_s velocity model; (b) NNW-SSE and (c) WSW-ESE cross-sections
 503 through the V_s velocity model (traces in a). Green arrow points north. See figure 3 to contextualize this figure in the
 504 workflow.

505

506 The V_p velocity model (Fig. 17) is mainly based on the DH recordings, plus some additional
 507 MASW (or seismic refraction profiles) and 2D array data (see table 1). For this reason, the lower
 508 part of the V_p model is less constrained compared to the V_s model. V_p values range between 225
 509 m/s (at the top of the S. Angelo 2D array) and 2960 m/s (maximum V_p value recorded the Cossito
 510 DH1). In the continental Quaternary units, we can observe a generally downward increasing of V_p
 511 values that, in this interval, vary from about 225 m/s to 1800 m/s (e.g., near the Quaternary base in
 512 the Amatrice DH2-San Cipriano and Amatrice DH3 Down-Holes). The Messinian foredeep
 513 deposits, instead, are characterized by greater V_p values, that approximately range from 317 m/s to
 514 2960 m/s, with several internal velocity inversions. In some areas, where the Laga unit crops out,
 515 we can observe low V_p values, like for example at the top of the San Capone DH1 Down-Hole (V_p
 516 =317 m/s).

517



518

519

520

521

522

523

524

525

526

527

528

529

530

531

532

533

534

535

Figure 17: 3D Vp velocity model. (a) View of the 3D Vp velocity model; (b) NNW-SSE and (c) WSW-ESE cross-sections through the Vp velocity model (traces in figure a). Green arrow points north. See figure 3 to contextualize this figure in the workflow.

4.4 Geophysical constraints

The model reliability has been estimated by comparing the experimental HVSR curves, available at the nearest seismic stations (i.e., MZ09 and CS19, localization in Fig. 5a), and the ellipticity curves calculated at the selected control points (i.e., Sommati DH1 and Amatrice historical centre, sites, Fig. 11).

The experimental HVSR curves, recorded at the nearest seismic stations, show two amplified frequency bands: a lowest frequency band (f_0), located between 1 and 2 Hz, with an associated HVSR peak with a value of about 4.2 at the two different control points (grey vertical bands in Fig.11), and a highest frequency band (f_1 , yellow vertical bands in Fig.11) ranging between 4.0 and 7.0 Hz, that in the case of Amatrice historical centre is characterized by a broadband behaviour and amplitude values of the HVSR smaller than 2.

The lowest amplified frequency band (f_0) has never been reproduced by the model and the ellipticity curves obtained at Sommati DH1 are characterized by large standard deviations. On the

536 contrary, all the amplification peaks at frequency between 4 and 7 Hz are recognizable in the
537 ellipticity curves. The averaged responses of the modeled ellipticity curves are only slightly
538 underestimated at high frequency (i.e., f_1), attesting the goodness of the model parameterization of
539 the surficial layers above 200 m. In fact, a bias affecting ellipticity amplitudes is expected and does
540 not invalidate the results: the natural noise field contains Love, Rayleigh and body waves, while the
541 calculated ellipticity is generated assuming that the noise field is composed only by Rayleigh
542 waves.

543 Looking at investigating the influence of lateral variability on the seismic response, ellipticity
544 curves obtained at the center of the two cylindrical meshes were also represented in Fig. 11.

545 In the two cases, at the centre of each model the ellipticity exceeds the average values \pm st. dev.

546 The case of Sommati site, where the ellipticity is significantly variable inside the modelled volume,
547 leads us to conclude that the geological variability is significant, although the HVSR measurement
548 is few meters away from the exact location of the Down-Hole.

549 In the historical centre, the variability is less evident, but ellipticity curve at the centre of the model
550 shows a slightly shift of the f_1 frequency respect to the average. The behaviour in this case confirms
551 that pinch-out zones, existing in the areas around the control points, influence the HVSR and the
552 ellipticity modelling, thus affecting also the actual seismic response at the sites.

553 **5 Discussions and conclusions**

554 The 2016-2017 seismic sequence, which violently struck central Italy, put in evidence that more
555 effort should be addressed to the assessment of the seismic hazard in the inner complex basins such
556 as the Amatrice Basin.

557 Structural and stratigraphic characterization of surface deposits allowed defining the local seismic
558 response (Chiaretti & Nibbi, 2018; EmerTer Project Working Group, 2018; Vignaroli et al., 2019;
559 Hailemikael et al., 2020; Mancini et al., 2020). Despite these studies have been the key for the
560 seismic hazard assessment of the area, they mainly investigate the characteristics of the shallow
561 subsoil layers, hampering a full three-dimensional parametrization of the geological volume
562 affected by the seismic waves. It should be noted that a three-dimensional geological model better
563 approximates geometries and latero-vertical heterogeneities (e.g., thickness, facies changing,
564 structural discontinuities) that induce modifications of the propagating seismic waves, in terms of
565 reflections, refractions, energy absorption, amplifications. For this reason, seismic hazard studies of
566 an area require realistic geological and seismic-velocity models. These models can provide more
567 accurate ground shaking predictions, as confirmed by the seismic hazard assessment studies carried
568 out by Magistrale et al. (1996) and Süß et al. (2001) in the Los Angeles sedimentary basin. The
569 authors proved that geology-based seismic-velocity models allow determining correctly the timing
570 and the amplitude of the arriving waves in earthquake ground-motion simulations.

571 After the 2016-2017 seismic sequence, a heterogeneous distribution of the damage was observed in
572 the Amatrice hamlet. The historical center, located at the northwest side of a terraced area, was
573 destroyed, while the central and southeastern portion of the village was affected by a lower damage.
574 Milana et al. (2019) highlighted a significant variability in the amplification function in terms of
575 both spectral ratio amplitude and frequency response. In particular, the authors observed a
576 vanishing of the amplification factors at the base of the Amatrice terrace and in central portion of
577 the village, while a strong amplification was observed in both the northwestern and the southeastern
578 edges. These variability in terms of effects highlights the possible contribution of the geological
579 heterogeneity, associated with topographic consequences near the terrace border.

580 In terms of novelty, our work provides an accurate geology-based velocity model, which
581 simultaneously considers geological and geophysical characteristics of the modeled volume. The
582 ellipticity curves, elaborated by extracting two cylindrical (75 m radius) V_s velocity meshes from
583 the whole V_s velocity model (Fig. 10), allows us identifying a high amplified frequency band (f_1),
584 between 4.0 and 7.0 Hz, where the calibration is satisfactory. In fact, this frequency band is also
585 amplified in the experimental HVSR curves recorded at the nearest seismic stations (Fig. 11). This

586 demonstrates not only the reliability of the realized geology-based V_s velocity model at the
587 calibrated sites, but also that the amplification of this frequency band originates within the last
588 hundreds of meters, within the modeled volume.

589 By employing our model in earthquake ground-motion simulations it could also be possible
590 predicting possible focusing and/or amplification effects, due to mechanical and geological features,
591 such as the upward concave geometries reconstructed beneath the Amatrice village (Fig. 14). In this
592 perspective, future research will be carried out.

593 In the experimental HVSR curves a lower amplified frequency band, f_0 , is recognized, but it was
594 never reproduced by means of our model (Fig. 11). The absence of the f_0 peak in the ellipticity
595 curves processed at the chosen sites could be due to: 1) the occurring of 2D/3D effect at low
596 frequency, such as recognized by Gaudiosi et al. (2021) along the Amatrice terrace; 2) the presence
597 of a deeper geological interface and/or mechanical impedance contrast, located below the modeled
598 volume.

599 Considering the results of our study, we can conclude as follows:

- 600 • our geology-based model could help in predicting correctly the amplitude and frequency of
601 arriving seismic waves by calibrating the model in additional scattered points of the
602 Amatrice Basin;
- 603 • the proposed model could also help in predicting possible focusing and/or amplification
604 effects by performing earthquake ground-motion simulations;
- 605 • a deepening of the model by using and interpreting data reaching greater depths, such as
606 seismic reflection profiles, is necessary to investigate the origin of the lowest amplification
607 frequency band (f_0);
- 608 • the proposed method represents a promising missing step between seismic zoning at large
609 scales and microzonation studies, by integrating all the available geological and
610 geophysical information;
- 611 • in complex geological contexts, such as the intermountain basins, the availability of
612 geophysical information linking surface and deep data is essential to correctly evaluate the
613 local seismic hazard;
- 614 • the proposed approach helps in defining more realistic seismic hazard scenarios and is
615 exploitable in other comparable sectors of the central Apennine.

616

617 **Appendix**

618 In this work a WGS84-UTM33N Spatial reference (EPSG 32633) has been adopted. For data
619 georeferencing we have used the QGis software (Version 2.18), while, for the realization of the 3D
620 geological model and its parameterization we have used the Petrel software (Version 2016.2), mark
621 of Schlumberger. Ellipticity curves have been modeled by using “gpell” code by geopsy software
622 (<http://www.geopsy.org/index.html>).

623 **Acknowledgments**

624 This work has been supported by the Institute of Environmental Geology and Geoengineering
625 (IGAG-CNR) of Rome, Italy [Research fellow, conferment document number 01543 dated 3 June
626 2019] and carried out within the framework of the AMATRIX project (a self-financed project as an
627 application of the RETRACE-3D project). Special thanks to the EmerTer Project Working Group
628 for making available geological and geophysical data underlying this work and for the useful
629 discussions and suggestions.

630

631 **References**

- 632 Aldega L., Botti F. & Corrado S. (2007) - *Clay mineral assemblages and vitrinite reflectance in the*
633 *Laga Basin (central Apennines Italy): what do they record?* Clay and Clay Minerals, 55,
634 504-518.
- 635 Argnani A. & Ricci Lucchi F. (2001) - *Tertiary siliciclastic turbidite systems of the Northern*
636 *Apennines*. In: G.B. Vai, & I.P. Martini, (Eds.), *Anatomy of an Orogen: the Apennines and*
637 *Adjacent Mediterranean Basins*. Kluwer Academic Publishers, 327-350.
- 638 Artoni A. (2003) - *Messinian events within the tectono-stratigraphic evolution of the Southern Laga*
639 *Basin (central Apennines, Italy)*. Boll. Soc. Geol. It., 122, 447-465.
- 640 Artoni A. (2007) - *Growth rates and two-mode accretion in the outer orogenic wedge-foreland*
641 *basin system of central Apennine (Italy)*. Boll. Soc. Geol. It., 126, 531-556.
- 642 Bigi S., Casero P., Corrado S., Milli S., Moscatelli M. & Stanzione O. (2006) - *Geometric*
643 *framework and thermal history of the Laga basin: constraints for integrated basin analysis*.
644 Abstract, Poster session Ts7.2 XY0592, EGU General Assembly 2006.
- 645 Bigi S., Milli S., Corrado S., Casero P., Aldega L., Botti F., Moscatelli M., Stanzione O., Falcini F.,
646 Marini M. & Cannata D. (2009) - *Stratigraphy, structural setting and thermal history of the*
647 *Messinian Laga Basin in the context of Apennine foreland basin system*. J. Met. Earth
648 Sciences, 1, 61-84.
- 649 Bigi S., Casero P. & Ciotoli G. (2011) - *Seismic interpretation of the Laga basin; constraints on the*
650 *structural setting and kinematics of the central Apennines*. Journal of the Geological
651 Society, London, 168, 179–190. doi:10.1144/0016-76492010-084
- 652 Billi A. & Tiberti M. (2009) - *Possible causes of arc development in the Apennines, central Italy*.
653 Geological Society of America Bulletin, 121, 1409–1420.
- 654 Boccaletti M., Ciaranfi N., Cosentino D., Deiana G., Gelati R., Lentini F., Massari F., Moratti G.,
655 Pescatore T., Ricci Lucchi F. & Tortorici L. (1990) - *Palinspastic restoration and*
656 *paleogeographic reconstruction of the peri-Tyrrhenian area during the Neogene*.
657 Paleogeography Paleoclimatology Paleoecology, 77, 41-50.
- 658 Boncio, P., Lavecchia, G. & Pace, B. (2004) - *Defining a model of 3D seismogenic sources for*
659 *Seismic Hazard Assessment applications: The case of central Apennines (Italy)*. Journal of
660 Seismology 8, 407–425. <https://doi.org/10.1023/B:JOSE.0000038449.78801.05>
- 661 Cacciuni A., Centamore E., Di Stefano R. & Dramis F. (1995) - *Evoluzione morfotettonica della*
662 *conca di Amatrice*. Studi Geologici Camerti, Volume speciale 1995 (2), 95–100.
- 663 Casero P. & Bigi S. (2006) - *Deep structure of the Laga Basin*. Abstract, Poster session TS7.2 -
664 XY0591, EGU General Assembly 2006.
- 665 [Data set] Castello B., Selvaggi G., Chiarabba C. & Amato A. (2006) - *CSI Catalogo Della*
666 *Sismicità Italiana 1981-2002, Version 1.1*. INGV-CNT, Roma.
- 667 Cavinato G. P. & De Celles, P. G. (1999) - *Extensional basins in the tectonically bimodal central*
668 *Apennines fold-thrust belt, Italy: Response to corner flow above a subducting slab in*
669 *retrograde motion*. Geology, 27, 955–958, doi:10.1130/0091-
670 7613(1999)027<0955:EBITTB>2.3.CO;2
- 671 Cavinato, G. P., Carusi, C., Dall'Asta, M., Miccadei, E. & Piacentini, T. (2002) - *Sedimentary and*
672 *tectonic evolution of Plio-Pleistocene alluvial and lacustrine deposits of Fucino Basin*
673 *(central Italy)*. Sedimentary Geology, 148, 29–59. doi:10.1016/S0037-0738(01)00209-3

- 674 Centamore E., Cantalamessa G., Micarelli A., Potetti M., Berti D., Bigi S., Morelli C. & Ridolfi M.
675 (1991) - *Stratigrafia e analisi di facies dei depositi del Miocene e del Pliocene inferiore*
676 *dell'avanfossa marchigiano-abruzzese e delle zone limitrofe*. Studi Geologici Camerti, vol.
677 spec. 1991/2, 125-131.
- 678 Centamore E., Cantalamessa G., Micarelli A., Potetti M., Berti D., Bigi S., Morelli C. & Ridolfi M.
679 (1992) - *Carta geologica del bacino della Laga e del Cellino e delle zone limitrofe*.
680 S.EL.CA., Firenze.
- 681 Chiaraluce L., Valoroso L., Piccinini D., Di Stefano R. & De Gori P. (2011) - *The anatomy of the*
682 *2009 L'Aquila normal fault system (central Italy) imaged by high resolution foreshock and*
683 *aftershock locations*. J. Geophys. Res., 116 (B12), doi: 10.1029/2011JB008352.
- 684 Chiaraluce, L., Di Stefano, R., Tinti, E., Scognamiglio, L., Michele, M., Casarotti, E., Cattaneo M.,
685 De Gori P., Chiarabba C., Monachesi G., Lombardi A., Valoroso L., Latorre D. &
686 Marzorati, S. (2017). *The 2016 central Italy seismic sequence: A first look at the*
687 *mainshocks, aftershocks, and source models*. Seismological Research Letters, 88(3), 757–
688 771. <https://doi.org/10.1785/0220160221>
- 689 Chiaretti F. & Nibbi L. (2018) - *Microzonazione Sismica di Livello 3 del Comune di Amatrice ai*
690 *sensi dell'ordinanza del Commissario Straordinario n°24 registrata il 15 maggio 2017 al*
691 *n°1065*. Comune di Amatrice, 2018.
692 http://www.regione.lazio.it/prl_ambiente/?vw=contenutidetail&id=238 (accessed 15
693 February 2021)
- 694 Cosentino D., Cipollari P., Marsili P. & Scrocca D. (2010) - *Geology of the central Apennines: a*
695 *regional review*. In: Beltrando M., Peccerillo A., Mattei M., Conticelli S. & Doglioni C.
696 (Eds.), *The Geology of Italy: tectonics and life along plate margins*, Journal of the Virtual
697 Explorer, volume 36, paper 12, doi: 10.3809/jvirtex.2010.00223.
- 698 Del Gaudio V., Wasowski J., Pierri P., Moretti A. & Ferrini G. (2021) - *Multitemporal analysis of*
699 *ambient noise polarization to characterize site response in the town of Amatrice, shattered*
700 *by the 2016 central Italy earthquake*. Geophys. J. Int. (2021) 224, 739–759. doi:
701 10.1093/gji/ggaa335
- 702 Deschamps A., Courboulex F., Gaffet S., Lomax A., Virieux J., Amato A., Azzara A., Castello B.,
703 Chiarabba C., Cimini G.B., Cocco, M., Di Bona M., Margheriti L., Mele F., Selvaggi G.,
704 Chiaraluce L., Piccinini D. & Ripepe M. (2000) - *Spatio-temporal distribution of seismic*
705 *activity during the Umbria-Marche crisis 1997*. J. Seismol., 4, 377–386.
- 706 Di Bucci D., Buttinelli M., D'Ambrogi C., Scrocca D. & RETRACE-3D Working Group (2021) -
707 *RETRACE-3D project: a multidisciplinary collaboration to build a crustal model for the*
708 *2016-2018 central Italy seismic sequence*. Bollettino di Geofisica Teorica ed Applicata, 62
709 (1), 1-18, doi: 0.4430/bgta0343.
- 710 Doglioni C. (1991) - *A proposal of kinematic modelling for west-dipping subductions - Possible*
711 *application to the Tyrrhenian-Apennines system*. Terra Nova, 3, 423-434.
- 712 EmerTer Project Working Group (2018) - *Report relativo all'Accordo ai sensi dell'art. 15 Legge 7*
713 *agosto 1990 n. 241, e dell'art.6 della Legge 24 febbraio 1992, n. 225 tra il Dipartimento*
714 *della Protezione Civile e l'Istituto di Geologia Ambientale e Geoingegneria del Consiglio*
715 *Nazionale delle Ricerche per il supporto alle attività della DICOMAC di Rieti e della*
716 *Struttura di Missione, 2018*. Prot. CNR IGAG n. 359 del 30/01/2018.
- 717 Fäh D., Kind F. & Giardini D. (2001) – *A theoretical investigation of average H/V ratios*.
718 Geophysical Journal International, 145, 535-549.
- 719

- 720 Galadini F., 1999. *Pleistocene changes in the central Apennine fault kinematics: A key to decipher*
721 *active tectonics in central Italy*. *Tectonics*, 18,5,, 877-894
722 <https://doi.org/10.1029/1999TC900020>.
- 723 Galadini, F. & Galli, P. (2003) - *Paleoseismology of silent faults in the central Apennines (Italy):*
724 *the Mt. Vettore and Laga Mts. faults*. *Annals of Geophysics*, 46(5), 815-836.
- 725 Galli P., Peronace E. & Tertulliani A. (2016) - *Rapporto sugli effetti macrosismici del terremoto del*
726 *24 Agosto 2016 di Amatrice in scala MCS*. Rapporto congiunto DPC, CNR-IGAG, INGV,
727 Roma. doi: 10.5281/zenodo.161323
- 728 Gaudiosi I., Simionato M., Mancini M., Cavinato G.P., Coltella M., Razzano R., Sirianni P.,
729 Vignaroli G., Moscatelli M. (2021) - *Evaluation of site effects at Amatrice (central Italy)*
730 *after the August 24th, 2016, Mw6.0 earthquake*. *Soil Dynamics and Erth. Eng.* 144.
731 <https://doi.org/10.1016/j.soildyn.2021.106699>
- 732 Giaccio, B., Galli P., Messina P., Peronace E., Scardia G., Sottili G., Sposato A., Chiarini E., Jicha
733 B. & Silvestri S. (2012) - *Fault and basin depocenter migration over the last 2 Ma in the*
734 *L'Aquila 2009 earthquake region, central Italian Apennines*. *Quaternary Sci. Rev.* 56, 69–
735 88. doi:10.1016/j.quascirev.2012.08.016
- 736 Grunis E.G. & Khasanov D.I. (2017) - *Reserves calculation using the volume and probability*
737 *methods with the aid oh Petrel-2013 program package*. *Methodology of prospecting and*
738 *exploration of oil and gas fields*, 5, 113-118.
- 739 Hailemikael S., Amoroso S. & Gaudiosi I. (2020) - *Guest editorial: seismic microzonation of*
740 *Central Italy following the 2016–2017 seismic sequence*. *Bull Earthquake Eng* 18, 5415-
741 5422. <https://doi.org/10.1007/s10518-020-00929-6>
- 742 Herrmann R.B., Malagnini L. & Munafò I. (2011) - *Regional moment tensor of the 2009 L'Aquila*
743 *earthquake sequence*. *Bull. Seismol. Soc. Am.* 101 (3), 975–993.
- 744 Improta L., Latorre D., Margheriti L. et al. (2019) - *Multi-segment rupture of the 2016 Amatrice-*
745 *Visso-Norcia seismic sequence ,central Italy, constrained by the first high-quality catalog of*
746 *Early Aftershocks*. *Sci Rep* 9, 6921. <https://doi.org/10.1038/s41598-019-43393-2>
- 747 [Data set] ISIDE Working Group (2007) - *Italian Seismological Instrumental and Parametric*
748 *Database (ISIDE)*. Istituto Nazionale di Geofisica e Vulcanologia (INGV).
749 <https://doi.org/10.13127/ISIDE>
- 750 Koopman, A. (1983) - *Detachment tectonics in the central Apennines*. *Geological Ultraiectina*, 30,
751 1–155.
- 752 Lavecchia G., Adinolfi G., De Nardis M., Ferrarini F., Cirillo D., Brozzetti F., De Matteis R., Festa
753 G. & Zollo A. (2017) - *Faulting model for the largest aftershock of the L'Aquila 1 2009*
754 *sequence and implications for unknown active extensional sources in central Italy*. *Terra*
755 *Nova* 29, 77–89, doi: 10.1111/ter.12251.
- 756 Lucente F.P., De Gori P., Margheriti L., Piccinini D., Di Bona M., Chiarabba C. & Agostinetti N.P.
757 (2010) - *Temporal variation of seismic velocity and anisotropy before the 2009 Mw 6.3*
758 *L'Aquila earthquake, Italy*. *Geology* 38 (11), 1015–1018.
- 759 Malinverno A. & Ryan W.B.F. (1986) - *Extension In the Tyrrhenian sea and shortening in the*
760 *Apennines as result of arc migration driven by sinking of the lithosphere*. *Tectonics*, 5, 227-
761 245.

- 762 Magistrale H., McLaughlin K. & Day S. (1996) - *A geology-based 3D velocity model of the Los*
763 *Angeles basin sediments*. Bulletin of the Seismological Society of America, 86 (4), 1161–
764 1166.
- 765 Mancini M., Cavuoto G., Pandolfi L., Petronio C., Salari L. & Sardella R. (2012) - *Coupling basin*
766 *infill history and mammal biochronology in a Pleistocene intramontane basin: The case of*
767 *western L'Aquila Basin (central Apennines, Italy)*. Quaternary International, 267, 62–77.
768 doi:10.1016/j.quaint.2011.03.020
- 769 Mancini M., Vignaroli G., Bucci F., Cardinali M., Cavinato G. P., Giallini S., Moscatelli M.,
770 Polpetta F., Putignano M. L., Santangelo M. & Sirianni P. (2020). *New stratigraphic*
771 *constraints for the Quaternary source-to-sink history of the Amatrice Basin (central*
772 *Apennines, Italy)*. Geol. J., 1–26. doi: 10.1002/gj.3672
- 773 Manzi V., Lugli S., Ricci Lucchi F. & Roveri M. (2005) - *Deep-water clastic evaporites deposition*
774 *in the Messinian Adriatic foredeep (Northern Apennines, Italy): did the Mediterranean ever*
775 *dry out?*. Sedimentology, 52, 875-902.
- 776 Marini M., Milli S., Ravnås R. & Moscatelli M. (2015) - *A comparative study of confined vs. semi-*
777 *confined turbidite lobes from the Lower Messinian Laga Basin (central Apennines, Italy):*
778 *implications for assessment of reservoir architecture*. Marine and Petroleum Geology, 63,
779 142-165. doi:10.1016/j.marpetgeo.2015.02.015
- 780 Marini M., Felletti F., Milli S., & Patacci M. (2016) - *The thick-bedded tail of turbidite thickness*
781 *distribution as a proxy for flow confinement: Examples from tertiary basins of central and*
782 *northern Apennines (Italy)*. Sedimentary Geology, 341, 96–118.
783 [https://doi:10.1016/j.sedgeo.2016.05.006](https://doi.org/10.1016/j.sedgeo.2016.05.006)
- 784 Mazzieri I., Stupazzini M., Guidotti R., Smerzini C. (2013) - *SPEED: Spectral Elements in*
785 *Elastodynamics with Discontinuous Galerkin: a non-conforming approach for 3D multi-*
786 *scale problems*. International Journal for Numerical Methods in Engineering 95, 12, 991–
787 1010.
- 788 Michele M., Chiaraluce L., Di Stefano R. & Waldhauser F. (2020) - *Fine-scale structure of the*
789 *2016-2017 central Italy Seismic Sequence from data recorded at the Italian National*
790 *Network*. Journal of Geophysical Research - Solid Earth. 10.1029/2019JB018440
- 791 Milana G., Cultrera G., Bordoni P., Bucci A., Cara F., Cogliano R., Di Giulio G., Di Naccio D.,
792 Famiani D., Fodarella A., Mercuri A., Pischiutta M., Pucillo S., Riccio G. & Vassallo M.
793 (2019). *Local site effects estimation at Amatrice (central Italy) through seismological*
794 *methods*. Bulletin of Earthquake Engineering, 1-27. [https://doi.org/10.1007/s10518-019-](https://doi.org/10.1007/s10518-019-00587-3)
795 00587-3
- 796 Milli S., Moscatelli M., Stanzione O. & Falcini F. (2007) - *Sedimentology and physical stratigraphy*
797 *of the Messinian turbidite deposits of the Laga Basin (central Apennines, Italy)*. Boll. Soc.
798 Geol. It., 126, 255-281.
- 799 Milli S., Moscatelli M., Marini M. & Stanzione O. (2009) - *The Messinian turbidite deposits of the*
800 *Laga basin (central Apennines, Italy)*. In: Pascucci V., Andreucci S. (Eds.), Field Trip
801 Guide Book, Post-conference trip FT12, 27th IAS Meeting of Sedimentology Alghero,
802 September 20-23, 2009, Sassari (Italy), 279-297.
- 803 Moscatelli M. (2003) - *La sedimentazione torbiditica e le sue relazioni con quella fluvio-deltizia nel*
804 *sistema d'avanfossa alto-miocenico dell'Appennino centro-meridionale*. Ph.D. Thesis,
805 Università di Roma “La Sapienza”.

- 806 Moscatelli M., Milli S., Stanzione O., Marini M., Gennari G. & Vallone R. (2004) - *I depositi*
807 *torbiditici del Messiniano inferiore dell'Appennino centrale: bacino del Salto-Tagliacozzo e*
808 *della Laga (Lazio, Abruzzo, Marche)*. II Congresso GeoSed, Roma 2004, Libro guida
809 dell'escursione post-congresso.
- 810 Moscatelli, I. Gaudiosi, R. Razzano, G. Lanzo, L. Callisto (2020) *Modellazione numerica*
811 *tridimensionale della risposta sismica dell'abitato di Amatrice*. Capitolo 2.1: Progetto
812 SISMI-DTC Lazio. Conoscenze e innovazioni per la ricostruzione e il miglioramento
813 sismico dei centri storici del Lazio. <https://doi.org/10.2307/j.ctv18phgdk>
- 814 Mutti E. & Ricci Lucchi F. (1972) - *Le torbiditi dell'Appennino settentrionale: introduzione*
815 *all'analisi di facies*. Mem. Soc. Geol. It., 11, 161-199.
- 816 Mutti E., Nilsen T.H. & Ricci Lucchi F. (1978) - *Outer fan depositional lobes of Laga Formation*
817 *(Upper Miocene and Lower Pliocene), east central Italy*. In: Stanley D.J. & Kelling G.,
818 (Eds.), *Sedimentation in submarine canyons, fans and trenches*. Downed, Hutchinson &
819 Ross, 210-223.
- 820 Mutti E. & Sonnino M. (1981) - *Compensation cycles: a diagnostic features of turbidite sandstone*
821 *lobes*. In: Valloni R., Colella A., Sonnino M., Mutti E., Zuffa G.G. & Ori G.G. (Eds.) IAS
822 2nd European Regional Meeting, Bologna, Abstract 120-123.
- 823 Nocentini M., Asti R., Cosentino D., Durante F., Gliozzi E., Macerola L. & Tallini M. (2017) -
824 *Plio-Quaternary geology of L'Aquila - Scoppito Basin (central Italy)*. Journal of Maps, 13
825 (2), 563–574. doi:10.1080/17445647.2017.1340910
- 826 Patacca E., Sartori R. & Scandone P. (1990) - *Tyrrhenian basin and Apenninic Arcs: Kinematic*
827 *relations since late Tortonian times*. Mem. Soc. Geol. It., 45, 425-451.
- 828 Pizzi A., Di Domenica A., Gallovič F., Luzi L. & Puglia R. (2017) - *Fault segmentation as*
829 *constraint to the occurrence of the main shocks of the 2016 central Italy seismic sequence*.
830 Tectonics, 36, 2370–2387. <https://doi.org/10.1002/2017TC004652>
- 831 Porreca M., Minelli G., Ercoli M., Brobia A., Mancinelli P., Cruciani F., Giorgetti C., Carboni F.,
832 Mirabella F., Cavinato G.P., Cannata A., Pauselli C. & Barchi M. R. (2018). *Seismic*
833 *reflection profiles and subsurface geology of the area interested by the 2016–2017*
834 *earthquake sequence (central Italy)*. Tectonics 37, 1116–1137. [https://doi:](https://doi.org/10.1002/2017TC004915)
835 10.1002/2017TC004915
- 836 Pucci S., Villani F., Civico R., Pantosti D., Del Carlo P., Smedile A., De Martini P.M., Pons
837 Branchu E. & Gueli A., (2015) - *Quaternary geology of the Middle Aterno Valley, 2009*
838 *L'Aquila earthquake area (Abruzzi Apennines, Italy)*. Journal of Maps, 11(5), 689–697.
839 doi:10.1080/17445647.2014.927128
- 840 Razzano R., Gaudiosi I., Moscatelli M., Luigi C., Lanzo G., Martini G., Hailemichael S. (2020)
841 *Modelling the three-dimensional site response in the village of Amatrice, Central Italy*.
842 Proceedings of the EGU Assembly, EGU2020-22483, [https://doi.org/10.5194/egusphere-](https://doi.org/10.5194/egusphere-egu2020-22483)
843 [egu2020-22483](https://doi.org/10.5194/egusphere-egu2020-22483)
- 844 RETRACE-3D Working Group (2021) - *RETRACE-3D: centRal italy EarThquakes integrATed*
845 *Crustal modEl. Rapporto finale di progetto*. Eds. INGV, ISPRA, CNR-IGAG, DPC. Roma,
846 pp. 100. doi: 10.5281/zenodo.4604940
- 847 Ricci Lucchi F. (1986) - *The Oligocene to recent foreland basin of the Northern Apennines*. In:
848 Allen P.A. & Homewood P., (Eds.). *Foreland basins*. IAS Spec. Publ., 8, 105-139.
- 849 Ripepe M., Piccinini D. & Chiaraluce L. (2000) - *Foreshock sequence of September 26th, 1997*
850 *Umbria-Marche earthquakes*. J. Seismol., 4 (4), 387–399.

- 851 Roveri M., Bassetti M.A. & Ricci Lucchi F. (2001) - *The Mediterranean Messinian salinity crisis: an Apennine foredeep perspective*. Sed. Geol., 140, 201-214.
852
- 853 Roveri M., Ricci Lucchi F., Lucente C.C., Manzi V. & Mutti E. (2002) - *Stratigraphy, facies and basin fill history of the Marnoso-Arenacea Formation*. In: Mutti E., Ricci Lucchi F. & Roveri M. (Eds.), *Revisiting turbidites of the Marnoso-arenacea Formation and their basinmargin equivalents: problems with classic models*. 64th EAGE Conference & Exhibition. Excursion Guidebook, University of Parma and ENI, AGIP Division, 1-26.
854
855
856
857
- 858 Roveri M., Manzi V., Ricci Lucchi F. & Rogledi S. (2003) - *Sedimentary and Tectonic evolution of the Vena del Gesso Basin (Northern Apennines, Italy): implications for the onset of the Messinian salinity crisis*. Geol. Soc. Am. Bull., 115, 387-405.
859
860
- 861 [Data set] Rovida A., Locati M., Camassi R., Lolli B. & Gasperini P. (2019) - *Catalogo Parametrico dei Terremoti Italiani (CPTI15), versione 2.0*. Istituto Nazionale di Geofisica e Vulcanologia (INGV). <https://doi.org/10.13127/CPTI/CPTI15.2>
862
863
- 864 [Data set] Rovida A., Locati M., Camassi R., Lolli B. & Gasperini P. (2020) - *The Italian earthquake catalogue CPTI15*. Bulletin of Earthquake Engineering. <https://doi.org/10.1007/s10518-020-00818-y>
865
866
- 867 Scisciani V. & Montefalcone R. (2005) - *Evoluzione neogenico-quadernaria del fronte della catena centro-appenninica: vincoli dal bilanciamento sequenziale di una sezione geologica regionale*. Boll. Soc. Geol. It., 124, 579-599.
868
869
- 870 Scognamiglio L., Tinti E., Michellini A., Dreger D.S., Cirella A., Cocco M., Mazza S. & Piatanesi A. (2010) - *Fast determination of moment tensors and rupture history: What has been learned from the 6 April 2009 L'Aquila earthquake sequence*. Seismol. Res. Lett., 81 (6), doi:10.1785/gssrl.81.6.892.
871
872
873
- 874 Scognamiglio, L., Tinti E. & Quintiliani M. (2016) - *The first month of the 2016 Amatrice seismic sequence: Fast determination of time domain moment tensors and finite fault model analysis of the ML 5.4 aftershock*. Ann. Geophys. 59, doi: 10.4401/ag-7246.
875
876
- 877 SESAME (2004) - *Guidelines for the implementation of the H/V spectral ratio technique on ambient vibrations: measurements, processing and interpretation*. SESAME European research project WP12 - Deliverable D23.12, European Commission - Research General Directorate, Bruxelles, Belgium.
878
879
880
- 881 Shao Y., Zheng A., He Y. & Xiao K. (2012) - *3D geological modeling under extremely, complex geological conditions*. J. Comput, 3, 699-705.
882
- 883 Smerzini C., Pitolakis K. (2018) - *Seismic risk assessment at urban scale from 3D physics-based numerical modeling: the case of Thessaloniki*. Bull Earthquake Eng 16, 2609–2631 <https://doi.org/10.1007/s10518-017-0287-3>
884
885
- 886 Stanzione O., Milli S., Moscatelli M. & Falcini F. (2006) - *Tectonic and climate control on turbidite sedimentation: the Messinian deposits of the Laga Formation (Central Italy)*. Abstract volume, Joint SEPM/Geological Society of London Conference: External controls on deep water depositional systems, climate, sea-level and sediment flux. London, 27-29 March 2006, 75-76.
887
888
889
890
- 891 Süß M.P., Shaw J. H.; Komatitsch D.; Tromp J. (2001) - *3D Velocity and Density Model of the Los Angeles Basin and Spectral Element Method Earthquake Simulations*. American Geophysical Union, Fall Meeting 2001, abstract id. S11A-0549
892
893
- 894 Tiberi Romano C. (1639) - *Nuova e vera relazione del terribile e spaventoso terremoto successo nella Città della Matrice e suo Stato*, Roma.
895

- 896 Valoroso, L., Chiaraluce L., Piccinini D., Di Stefano R., Schaff D. & Waldhauser F. (2013) -
897 *Radiography of a normal fault system by 64,000 high-precision earthquake locations: The*
898 *2009 L'Aquila (central Italy) case study*. J. Geophys. Res., 118 (3), 1156–1176.
- 899 Vignaroli G., Mancini M., Bucci F., Cardinali M., Cavinato G.P., Moscatelli M., Putignano M.L.,
900 Sirianni P., Santangelo M., Ardizzone F., Cosentino G., Di Salvo C., Fiorucci F., Gaudiosi
901 I., Giallini S., Messina P., Peronace E., Polpetta F., Reichenbach P., Scionti V., Simionato
902 M. & Stigliano F. (2019) - *Geology of the central part of the Amatrice Basin (central*
903 *Apennines, Italy)*. Journal of Maps, 15 (2), 193-202. doi: 10.1080/17445647.2019.1570877
- 904 Vignaroli G., Mancini M., Brilli M., Bucci F., Cardinali M., Giustini F., Voltaggio M., Yu T.-L. &
905 Shen C.-C. (2020) - *Spatial- temporal evolution of extensional faulting and fluid circulation*
906 *in the Amatrice Basin (central Apennines, Italy) during the Pleistocene*. Frontiers in Earth
907 Science, 8, 130. <https://doi.org/10.3389/feart.2020.00130>
- 908 Wathelet, M (2005) - *Array recordings of ambient vibrations: surface-wave inversion*. PhD
909 Dissertation, Liège University, 177p.
- 910
911
- 912